Icarus 197 (2008) 480–496

Contents lists available at ScienceDirect

Icarus

www.elsevier.com/locate/icarus

Triaxial ellipsoid dimensions and rotational poles of seven asteroids from Lick Observatory adaptive optics images, and of Ceres

Jack Drummond [a,*], Julian Christou [b,1]

[a] Starfire Optical Range, Directed Energy Directorate, Air Force Research Laboratory, Kirtland AFB, NM 87117-5776, USA
[b] Division of Astronomical Sciences, National Science Foundation, Arlington, VA 22203, USA

ARTICLE INFO

Article history:
Received 7 September 2007
Revised 6 May 2008
Available online 3 June 2008

Keywords:
Asteroids
Adaptive optics

ABSTRACT

Seven main belt asteroids, 2 Pallas, 3 Juno, 4 Vesta, 16 Psyche, 87 Sylvia, 324 Bamberga, and 707 Interamnia, were imaged with the adaptive optics system on the 3 m Shane telescope at Lick Observatory in the near infrared, and their triaxial ellipsoid dimensions and rotational poles have been determined with parametric blind deconvolution. In addition, the dimensions and pole for 1 Ceres are derived from resolved images at multiple epochs, even though it is an oblate spheroid.

Published by Elsevier Inc.

1. Introduction

We reintroduce a method to find an asteroid's triaxial ellipsoid dimensions and rotational pole from resolved images in just one or two nights, and then apply the method to seven asteroids observed in 2004 and 2006 with adaptive optics (AO) using the natural guide star system on Lick Observatory's 3 m telescope. Before addressing the seven asteroids individually, we discuss the equations and principles involved in converting the apparent size, shape, and orientation of resolved asteroids to their triaxial ellipsoid dimensions and rotational pole, and then we discuss the special case of Ceres, an oblate spheroid. In light of the anticipated DAWN mission to Ceres and Vesta, we expand the discussion of Vesta to derive a consensus model based on the dimensions and poles from all fourteen high resolution observation sets of Vesta made with speckle interferometry (SI), AO, and the Hubble Space Telescope (HST), including a heretofore unpublished analysis of HST observations made in 1997. The final section summarizes the results, including an illustrative comparison between the asteroids and the point spread functions.

2. Ellipses projected by triaxial ellipsoids

2.1. Analytic methods

The equations necessary for converting the changing apparent size, shape and orientation of an asteroid as it rotates to its triaxial dimensions and pole was first derived by Drummond et al. (1985) and applied to speckle interferometry observations of Asteroid 433 Eros. The full prescription was again given later by Drummond (2000). In this paper, however, we only describe the method qualitatively in order to illustrate the principles. Under the basic assumption that an asteroid can be modeled as a smooth featureless triaxial ellipsoid with diameters $a > b > c$ rotating about its short axis, then as it rotates it will project a series of ellipses of apparent major axes α and minor axes β, where the long axis will make an angle γ with the line of nodes, the intersection of the asteroid's equatorial plane and the plane of the sky.

There are six unknowns to find over the course of several rotations, the three axes dimensions a, b, and c, and three angles, ψ_0, the rotational zero point, θ, the asterocentric sub-Earth latitude, and the obliquity ρ, the angle that the Sun makes with the line of nodes. Since the position angle of the Sun with respect to celestial North (NtS) is known at any time for any observation and which we can regard as fixed over a few rotations, and since we can measure the position angle (pa_α) of the long axis of the asteroid, we can determine the position angle for the line of nodes as

$$NtS + \rho = pa_\alpha - \gamma, \tag{1}$$

where γ, like the other two observables α and β, is a function of five of the six unknowns. The three observables change as a function of the rotational phase ψ and the unknowns

$$[\alpha, \beta, \gamma] = f(\psi) = f(a, b, c, \psi_0, \theta), \tag{2a}$$

$$pa_\alpha = f(\psi) = \gamma + \rho + NtS, \tag{2b}$$

where $\psi = \psi_r - \psi_0$, and where ψ_r is the arbitrary relative rotational phase determined with a known rotational period and ψ_0

* Corresponding author.
E-mail address: Jack.Drummond@kirtland.af.mil (J. Drummond).
[1] On leave from Center for Adaptive Optics, University of California, Santa Cruz, CA 95064-1077, USA.

0019-1035/$ – see front matter Published by Elsevier Inc.
doi:10.1016/j.icarus.2008.05.009

is the rotational zero point, one of the six unknowns to be determined in the fit.

Twice each rotational period, at $\psi = 0$ and 180°, α reaches its maximum because a lies unprojected in the plane of the sky along the line of nodes, i.e., $\alpha = a$. At this instant, $pa_\alpha = NtS + \rho$, and, therefore, from Eq. (1), $\gamma = 0$. A quarter of a rotation later b lies unprojected in the plane of the sky along the line of nodes. If

$$\cos\theta^2 < \left(a^2 - b^2\right)/\left(a^2 - c^2\right), \tag{3}$$

then the position angle of the long axis will rotate through 360° during one period, but if

$$\cos\theta^2 > \left(a^2 - b^2\right)/\left(a^2 - c^2\right), \tag{4}$$

then pa_α will reverse directions as the asteroid rotates, oscillating about the line of nodes. For the maximum ($\psi = 0, 180$) and minimum ($\psi = 90, 270$) of the cross-sectional area, or lightcurve, Eq. (5) summarizes the situation.

$$\begin{aligned}
&\alpha(\psi = 0, 180) = a,\\
&\beta(\psi = 0, 180) = \sqrt{b^2\sin^2\theta + c^2\cos^2\theta},\\
&pa_\alpha(\psi = 0, 180) = NtS + \rho,\\
&\alpha(\psi = 90, 270) = \max\left(b, \sqrt{a^2\sin^2\theta + c^2\cos^2\theta}\right),\\
&\beta(\psi = 90, 270) = \min\left(b, \sqrt{a^2\sin^2\theta + c^2\cos^2\theta}\right),\\
&pa_\alpha(\psi = 90, 270) = NtS + \rho + 90 \quad \text{for Eq. (3) if } \theta > 0\\
&\qquad\qquad\qquad\quad = NtS + \rho - 90 \quad \text{for Eq. (3) if } \theta < 0\\
&\qquad\qquad\qquad\quad = NtS + \rho \quad \text{for Eq. (4).}
\end{aligned} \tag{5}$$

The full set of equations for all ψ is given in the above references. Thus, once ψ_0 is determined from the changing orientation and shape, a, b, and ρ can be observed directly at certain rotational phases [Eq. (5)]. The remaining two unknowns are closely tied together. Notice in Eq. (5) that c only appears with $\cos\theta$. However, from an evaluation of the full set of equations throughout the rotation, c and $\cos\theta$ can be separated, although they remain correlated.

Further insight can be gained by considering some boundary conditions. If the observer is in the asteroid's equatorial plane ($\theta = 0$), then according to Eq. (5), c is directly observed as β at all times, α changes between a and b, and pa_α never changes, defining the line of nodes. If the observer is over the asteroid's south rotational pole ($\theta = -90$), then $\alpha = a$, $\beta = b$, pa_α rotates smoothly through 360°, and because θ is −90°, the position of the pole coincides with the position of the asteroid. However, c is indeterminate for this geometry.

There are also some degenerate cases that can cause least squares fitting to fail altogether. For example, if the asteroid is an oblate spheroid ($a = b$), then no observable changes with rotation. However, $\alpha = a = b$, yielding two of the unknowns, and the constant position angle of the long axis defines the line of nodes ($pa_\alpha = NtS + \rho$). The rotational phase zero point has no meaning, and $\beta = \sqrt{a^2\sin^2\theta + c^2\cos^2\theta}$, which does not allow c or θ, and thus the pole, to be determined. However, if another image of this oblate spheroid is obtained when the asteroid is at a different position, then the pole and c can be determined. The rotational pole will lie at the intersection of the two great circles that run perpendicular from the line of nodes of the asteroid at the two (or more) positions. There is a two-fold ambiguity associated with this method because there are actually two possible intersections 180° apart. For either case, θ can be calculated, and c from Eq. (5), with $\beta = \sqrt{a^2\sin^2\theta + c^2\cos^2\theta}$.

Table 1
Observed oblate spheroid parameters for ceres

Ref.	Date	RA (°); Dec (°)	α (km)	β (km)	pa_β (°)
HST 2003[a]	Dec 28, 2003	114; +29	958 ± 2	896 ± 2	5 ± 1
HST 1995[b]	Jun 25, 1995	156; +20	970 ± 10	932 ± 12	4 ± 15
SOR[c]	Sep 19, 1993	38; +1	990 ± 40	884 ± 22	325 ± 9
St Pe[d]	May 5, 1991	206; +3	998 ± 42	938 ± 40	37 ± 7
Occ[e]	Nov 13, 1984	48; +9	960 ± 4	906 ± 10	331.5 ± 6
Keck[f]	Sep 22, 2002	18; −9	959 ± 5	890 ± 4	338 ± 2

[a] This paper.
[b] Parker et al. (2002).
[c] Drummond et al. (1998).
[d] Saint-Pe et al. (1993).
[e] Millis et al. (1987).
[f] Carry et al. (2008).

2.2. Oblate spheroid Asteroid 1 Ceres

As an example of an oblate spheroid, consider the case of Ceres, which, despite being the largest asteroid, did not have its rotational pole definitively determined until the Hubble Space Telescope observed a feature crossing its face (Thomas et al., 2005; see also Parker et al., 2002 and Li et al., 2006). Recently, Carry et al. (2008) similarly derived its pole and dimensions from AO with the Keck 10 m telescope.

Although Drummond et al. (1998) observed it with AO on a 1.5 m telescope, and derived a triaxial ellipsoid shape, they obviously interpreted noisy measurements as indicating changing shape. However, the line of nodes was well determined as the mean position angle of its long axis in their observations. The apparent major and minor axes dimensions and the position angle of the perpendicular to the line of nodes, pa_β, are given in Table 1 for their observations, as well as similar parameters from five other observations, a stellar occultation observed in 1984, infrared observations in 1991, two sets of HST observations, and Keck 10 m AO observations in 2008. For the latter, the 2° error on the pa_β in Table 1 corresponds to the difference between the $pa_\beta = 336°$ we predict with the pole they derive and the 338° they report.

The first entry in Table 1 comes from a study of 12 HST pipeline calibrated 1 s images of Ceres observed in 2003 at 5500 Å (where it appeared featureless), kindly provided by Joel Parker (personal communication). This a subset of the data used by Thomas et al. (2005). After using parametric blind deconvolution, described in the next section, to find the apparent ellipse long and short dimensions and orientation for each image, we attempted to fit for a triaxial ellipsoid parameters, but obtained poor results because it is closer to an oblate spheroid than a triaxial ellipsoid. Therefore, we assumed that $a = b = \bar{\alpha}$ and formed the mean and standard deviations of the long and short dimensions and position angles as reported in Table 1.

Fig. 1 shows the great circles in the direction of pa_β drawn from the position of the asteroid on the given dates. A weighted mean of the 15 intersections is at [RA; Dec] = [293; +63], with a radius error of $\sigma = 4°$, indicated in Fig. 1 by the circle of uncertainty. The weights used to calculate the mean are inversely proportional to the area in steradians of uncertainty around each intersection, which is calculated from

$$(1 - \cos\sigma)\pi/2 = [\phi_1 \sin d_1 \sin\phi_2 + \phi_2 \sin d_2 \sin\phi_1]/2\sin\epsilon, \tag{6}$$

where ϕ is the uncertainty in the position angle of the short (or long) axis from Table 1, d is the angular distance between the observation and the intersection, and ϵ is the acute angle of the intersection. It is interesting to note that the position of this new pole falls in the middle of three significant intersections in Fig. 1, two places where three great circles intersect, and the Keck and HST 2005 intersection, the two best determined poles.

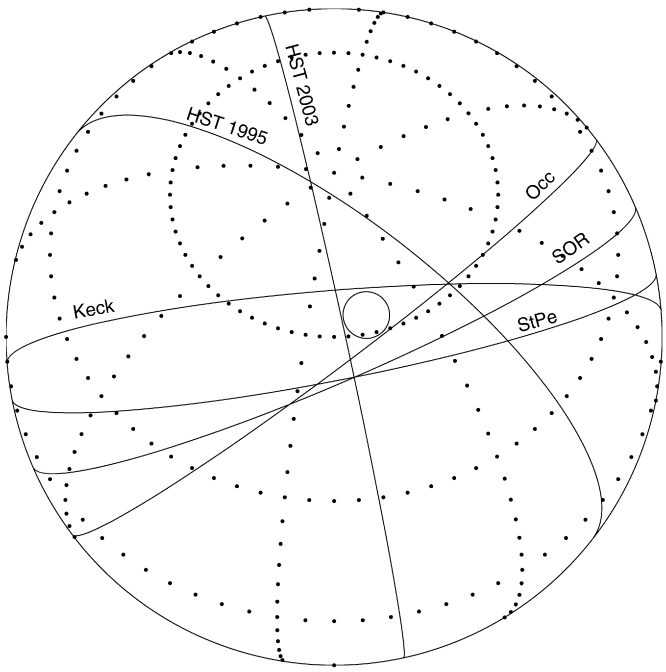

Fig. 1. Great circles on the celestial (not Ecliptic as for the remainder of such figures) globe, containing the position of Ceres and its pole for six data sets. All of the great circles should intersect at the true position of Ceres' pole, which we estimate to be within 4° of [293; +63].

Using $a = \bar{\alpha} = 973 \pm 7$ from the six epochs in Table 1, and calculating $c = \sqrt{\beta^2 - a^2 \sin^2\theta}/\cos\theta$ for each observed β and back-calculated θ, we find an average c of 908 ± 9 km. There is the possibility that this is Ceres' south pole, but resolved images clearly show that this is the north pole. By following a feature across the face of Ceres in the 2003 HST images, Thomas et al. (2005) derived a pole at [291; +59], $a = b = 974.6 \pm 3.6$, and $c = 909.4 \pm 3.6$ km, all in excellent agreement. Carry et al. (2008) find the pole at [288; +66], and dimensions of $a = b = 959.4 \pm 4.6$ and $c = 888.8 \pm 4.2$ km. Our result for Ceres, which, to our knowledge, represents the first use of this technique of intersecting great circles, are included in the final table of this paper, along with the dimensions and poles for all of the other asteroids to follow.

3. Seven triaxial ellipsoid asteroids

3.1. Parametric blind deconvolution

Our method of pulling the size, shape, and orientation of an asteroid from an adaptive optics (AO) image is termed parametric blind deconvolution (PBD) because it does not require a separate measurement of the point spread function (PSF) since it has been determined that the PSF for AO is Lorentzian in overall shape (Drummond, 1998; Drummond et al., 1998). The convolution of the Lorentzian and the asteroid can best be least squares fit in the Fourier plane, where it becomes the product of a Bessel function of the second kind of order 0, K_0, for the Lorentzian, and a Bessel function of the first kind of order 1, J_1, for the asteroid. A nonlinear least squares fit then yields the asteroid's apparent major and minor axes dimensions and the position angle of the long axis, and the same quantities for the Lorentzian PSF. If the image has already been deconvolved of the PSF, then the image can be fit in the Fourier plane for only the asteroid.

Using the natural guide star (NGS) AO system on the Shane 3 m telescope at Lick Observatory on Mt. Hamilton near San Jose, California, seven asteroids were observed over two or three consecutive nights on three runs in 2004 and 2006, interspersed with binary star measurements (Christou and Drummond, 2006). The Lick AO system uses the IRCAL near-infrared imager (Lloyd et al., 2000) behind a 127-actuator (61 actively controlled) deformable mirror. Since the asteroids were bright enough ($V < 11$), they were used for both AO corrections employing a Shack–Hartmann wavefront sensor and fast-read CCD camera, and tip-tilt corrections using a photodiode quad cell. Additional information on the Lick AO system is given by Bauman et al. (2002) and Gavel et al. (2000).

Table 2
Shane telescope ($D = 3$ m) filter parameters

Filter	λ_0 (μm)	FWHM (μm)	λ/D (″)
J	1.238	0.271	0.085
H	1.656	0.296	0.114
K_S	2.150	0.320	0.148
HI	2.167	0.020	0.149

Table 3
Asteroid observing log

Asteroid	RA (°)	Dec (°)	V	NtS (°)	ω (°)	Δ (AU)	r (AU)	km/mas
August 29, 2004								
3 Juno	279	−10	10.1	275	17.3	2.225	2.887	1.614
4 Vesta	359	−12	6.2	96	8.9	1.383	2.353	1.003
16 Psyche	310	−17	9.8	257	10.4	1.749	2.679	1.262
87 Sylvia	348	−22	11.4	142	5.0	2.230	3.213	1.617
324 Bamberga	297	−26	9.7	254	19.8	1.159	2.020	0.841
February 12, 2006								
3 Juno	76	+6	8.8	257	26.0	1.521	2.096	1.103
4 Vesta	99	+25	7.1	275	16.0	1.717	2.515	0.849
16 Psyche	70	+19	10.8	261	19.9	2.270	2.748	1.646
July 18, 2006								
2 Pallas	274	+22	9.6	330	13.3	2.564	3.323	1.860
704 Interamnia	333	+7	10.9	50	15.2	1.924	2.739	1.395

With an image scale of $0.076 \pm 0.001''$/pix, supplied by the observatory and confirmed in our own measurements of several binary stars (Christou and Drummond, 2006), observations were made through one of the four filters listed in Table 2. Every image was sky-subtracted, but not edited for bad pixels or flat-fielded since the fits are made in the Fourier domain where such minor localized image domain defects are distributed over the whole field, making the fits quite robust.

The observing log is listed for each asteroid in Table 3, where the 2000 position and V magnitudes are from JPL's Horizon system, and where NtS is, in the direction of the asteroid, the position angle of the Sun measured East from North, ω is the solar phase angle, Δ is the asteroid–Earth distance in AU, and r is the asteroid–Sun distance. The scale at the asteroid's distance is also given in km/mas.

3.2. Uncertainties

Finding asteroid sizes in the image domain would involve trying to find sub-pixel discontinuities (edges) at some point, which is a process that is not amenable to least squares fitting. However, in the Fourier domain, the asteroid appears as a sinusoidal function over typically 64×64 pixels, making it much easier to find the nine unknown parameters that describe the asteroid (α, β, pa_α, the center x_0 and y_0, and the amplitude) and the Lorentzian PSF (α_L, β_L, and $pa_{L\alpha}$). Fig. 2 shows the fits for a well resolved asteroid, Vesta in 2004, and Fig. 3 for a poorly resolved asteroid, Interamnia in 2006.

The uncertainties in the parameters from the least squares fit in the Fourier plane are usually very small, much smaller than the differences between the five successive measurements on the chip. Therefore, either a weighted mean is formed for the five measurements, or they are all entered individually into another least

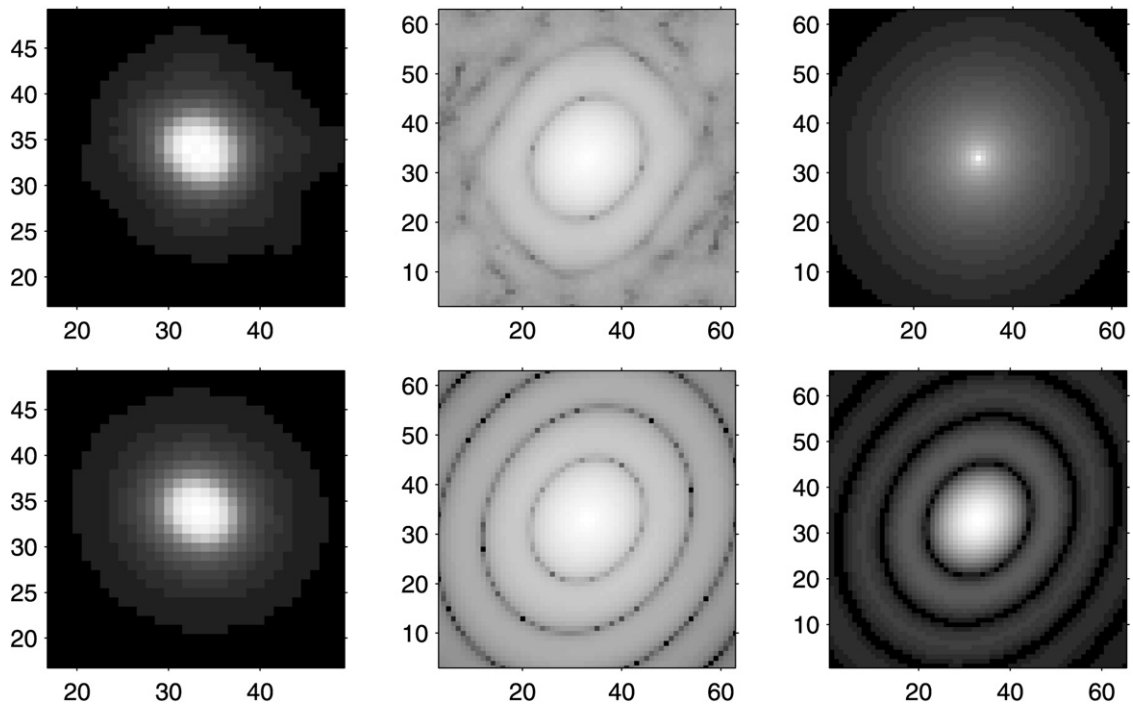

Fig. 2. Fitting example for Vesta. One of the 2 s images of Vesta on August 30, 2004, is shown at upper left. The fit is made of the FFT of the image, but the logarithm of the magnitude of the FFT of the image is displayed at upper middle in order to better show detail. The logarithm of the magnitude of the FFT of the Lorentzian PSF is shown at upper right and of the model asteroid at lower right, both obtained from a least squares fit of the upper middle frame. The multiplication of the upper and lower right frames results in the lower middle frame, the fit to the upper middle frame, and taking the inverse FFT of this fit results in the image domain display of the fit at lower left. The scale is pixels. Vesta is well resolved as revealed by the multiples zeros in the middle frames.

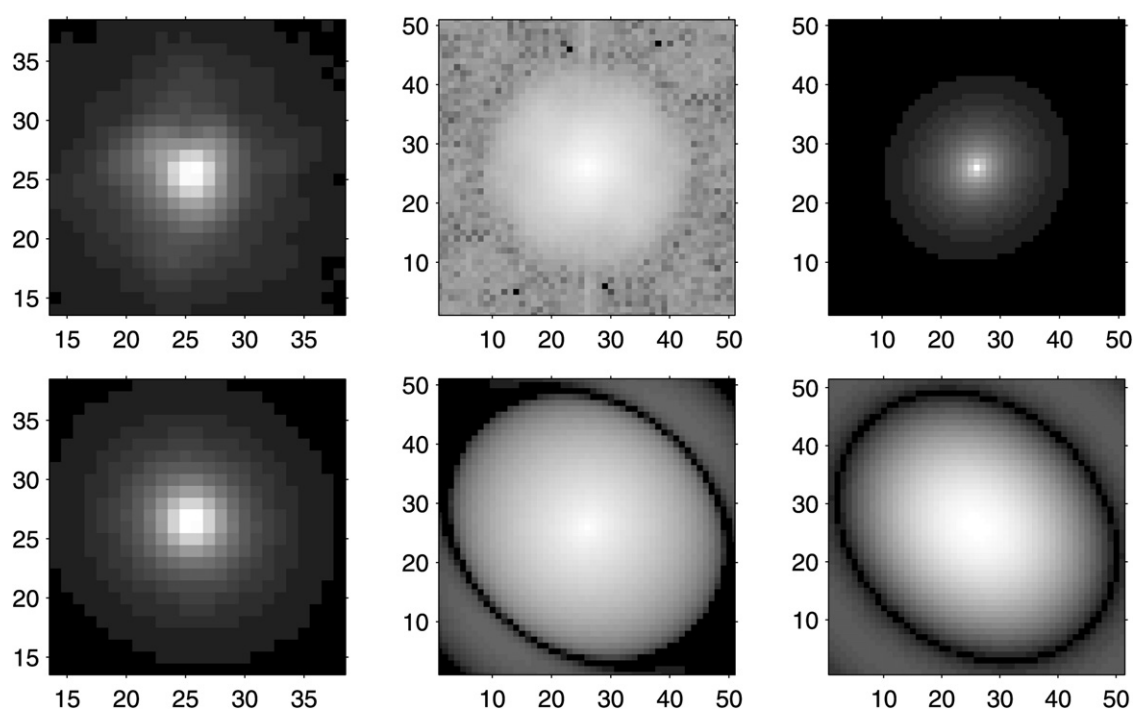

Fig. 3. Same as Fig. 2, except for Interamnia (15 s exposure) on July 18, 2006. The asteroid's first zero crossing in the Fourier domain at bottom right and bottom center falls just outside the high frequency cutoff, the beginning of the noise in the actual FFT in the upper middle frame. The fit is restricted to inside the high frequency cutoff, but the size can still be found from the fit to the model over this range.

squares program that produces triaxial ellipsoid parameters from the apparent ellipses observed over the course of a few rotations. The final uncertainties are produced directly by this least squares fit and are based on the residuals which contain contributions both from measurement errors and from departures from the triaxial ellipsoid assumption. Thus, in what follows, individual plots that show uncertainties are illustrating the precision of the measurements.

The uncertainties obtained by combining different independent analyses (Table 6) or oppositions (Table 7) are errors of the means of the parameters. Finally, the 1.3% uncertainty in the image scale represents a possible systematic uncertainty in all of

Table 4
Asteroid ellipsoid parameter results

Name	a (km)	b (km)	c (km)	θ (°)	N (°)	ψ_0 (UT)
August 29, 2004						
3 Juno	315 ± 22	249 ± 9	192 ± 75	+41 ± 20	271 ± 4	0.868 ± 0.047
4 Vesta	559 ± 2	543 ± 2	436 ± 18	−27 ± 8	237.7 ± 0.3	5.941 ± 0.048
16 Psyche	289 ± 6	267 ± 6	197 ± 4	−1 ± 8	350 ± 1	3.827 ± 0.128
87 Sylvia	350 ± 19	264 ± 14	227 ± 33	+29 ± 15	300 ± 4	9.094 ± 0.007
324 Bamberga	215 ± 15	199 ± 7	199 ± 7	+8 ± 18	105 ± 18	12.4 ± 1.4
February 11, 2006						
3 Juno	297 ± 6	233 ± 5	222 ± 6	−26 ± 5	309 ± 3	2.403 ± 0.082
4 Vesta	555 ± 12	531 ± 6	221 ± 622	+54 ± 24	245 ± 3	4.473 ± 0.087
4 Vesta[a]			442 ± 7	+21		
16 Psyche	327 ± 8	314 ± 4	188 ± 135	−54 ± 20	189 ± 2	2.396 ± 0.053
July 18, 2006						
2 Pallas	594 ± 17	549 ± 15	369 ± 128	+33 ± 23	354 ± 2	5.960 ± 0.213
704 Interamnia	385 ± 53	337 ± 21	163 ± 184	−34 ± 33	335 ± 4	8.926 ± 0.342

[a] Assumes $\theta = 21°$ from HST pole.

Table 5
Asteroid ellipsoid poles

Name	Eq.		Pole	Ecl	
	RA (°)	Dec (°)	Err Rad (°)	Lon (°)	Lat (°)
August 29, 2004					
3 Juno	97	+58	9	95	+35
4 Vesta	321	+40	1.6	342	+51
16 Psyche	36	+9	3	36	−5
87 Sylvia	100	+62	8	96	+39
324 Bamberga	142	−53	20	177	−62
February 11, 2006					
3 Juno	133	+47	4	122	+29
4 Vesta	294	+8	8	297	+29
16 Psyche	31	+20	6	36	+7
July 18, 2006					
2 Pallas	37	−7	6	32	−21
704 Interamnia	29	+25	11	36	+12

our measurements, but is not included in our quoted uncertainties.

3.3. Lightcurves

Perhaps the most fundamental datum for an asteroid is a lightcurve. Lightcurves obtained from many oppositions can lead to an asteroid's triaxial ellipsoid axial ratios (but not dimensions) and pole with a variety of techniques, all summarized by Magnusson et al. (1989). Magnusson (1989) began compiling axial ratios and poles for asteroids, and that compilation is now maintained on a web site at Poznan Observatory by A. Kryszczynska,[2] who also offers a consensus of values for the axial ratios, poles, and rotational sidereal periods.

There is normally a two-fold or four-fold pole ambiguity inherent in lightcurve techniques that is roughly symmetric with respect to the asteroid's orbit (Magnusson et al., 1989), but this is different than the two-fold pole ambiguity associated with PBD on one date, which is symmetric with respect to the position of the asteroid on that date. However, with AO observations on two significantly different dates the ambiguity can be resolved. Or, by appealing to the ambiguous lightcurve poles, it is often possible to resolve the AO ambiguity from observations on only one date. At any rate, it is instructive to compare the predictions from any model to actual individual lightcurves. In what follows, we resolve poles by either using the lightcurve pole solutions, or we have made sets of observations at two different oppositions. We will also compare our results to Kryszczynska's compilation and consensus values.

The uncertainties in our pole position from PBD arises from the uncertainty in determining the line of nodes and the asterocentric sub-Earth latitude, θ. Thus the actual shape of the pole uncertainty is wedge shaped. In previous work we have quoted the pole uncertainty as a radius of uncertainty. Here we will display both the wedge and the circle of uncertainty around the pole, when they are distinguishable, but we continue to use a radius of uncertainty in the tables. They both have the same area.

3.4. Individual asteroids

Table 4 gives the triaxial ellipsoid fit parameters for each observational set for each asteroid. The triaxial ellipsoid diameters are given in km, θ is the asterocentric sub-Earth latitude at the time of the observations, N is the position angle of the line of nodes, and ψ_0 is the lighttime corrected time of maximum cross-sectional area, which should also correspond to a maximum in a lightcurve, as well as the time when a lies unprojected in the plane of the sky along the line of nodes.

Table 5 gives the rotational pole locations from each fit. Both celestial and Ecliptic coordinates are given for epoch J2000. As discussed in the last section, the error radius that is given corresponds to a circle with the same area as the actual wedge shaped region of uncertainty.

For each asteroid discussed next, we show the triaxial ellipsoid fit to the data, and the location of the variously determined rotational poles. In the figures showing the triaxial ellipsoid fit, the data are shown as symbols, the apparent ellipse parameters projected by the triaxial ellipsoid model are shown as solid lines, and the apparent terminator ellipse parameters are shown as dashed lines. At low solar phase angles the two will merge and may become indistinguishable, but the data should fall between the two. In the upper subplot of each triaxial fit figure, the apparent long diameters are plotted along the upper line and the short axes along the lower line. The lower subplot shows the fit for the position angle of the long axis, with the straight solid line across the diagram marking the position of the line of nodes, 90° from the direction to the pole. All of the figures are lighttime corrected back to the asteroid.

Since the asteroids were recorded at five different positions on the chip at each rotational phase, each was fit separately, and the mean parameters and standard deviations are what is plotted in some cases, or all of the measurements in others. The range is the same for all figures, 300 km for the upper subplots (except that one figure for Vesta has a range of 600 km in order to include the Lorentzian PSF sizes), and for the lower subplots either 45° for low amplitude variation with small scatter, or 180° for asteroids that rotate through 360°, have large amplitude variations, or show large scatter.

The pole location figures show the poles from Kryszczynska's compilation as small circles, and an error circle and wedge around our pole, all on an Ecliptic globe. The circle and wedge have the same area.

3.4.1. 2 Pallas

Being large and bright, Pallas has been observed often and has many estimates of its pole direction, but with little consensus, although Kryszczynska does consider the ambiguity broken. We observed Pallas through the K_S filter in July 2006, and although the a and b dimensions are determined to within 3%, because its size was comparable to the PSF the results for θ and c, which are always coupled, are obtained with rather large uncertainties. Tables 4 and 5 contain our results for Pallas, Fig. 4 illustrates the triaxial ellipsoid fit to our observations, and Fig. 5 shows all of the pole estimates. Despite the large uncertainty in our pole

[2] http://vesta.astro.amu.edu.pl/Science/Asteroids/.

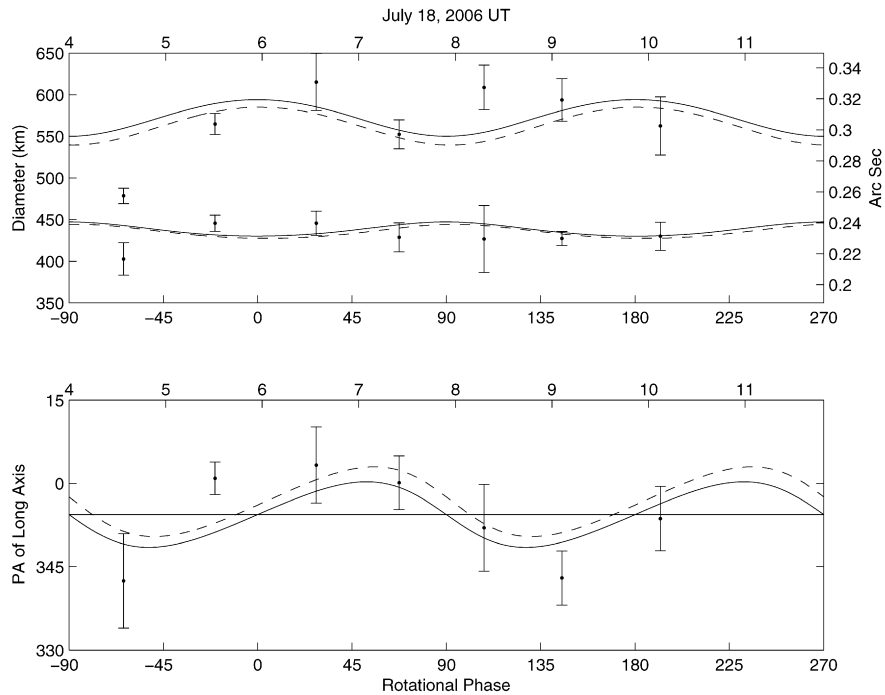

Fig. 4. Triaxial ellipsoid fit for Pallas. The mean Lorentzian PSF diameter was $0.24'' \pm 0.03$, comparable to the size of the asteroid in the upper subplot. In the lower subplot, the position angle of the long axis varies around the line of nodes at 354°. Rotational phase zero corresponds to July 18, 2006, 5.96 UT (lighttime corrected), using a rotational period of 7.8132 h.

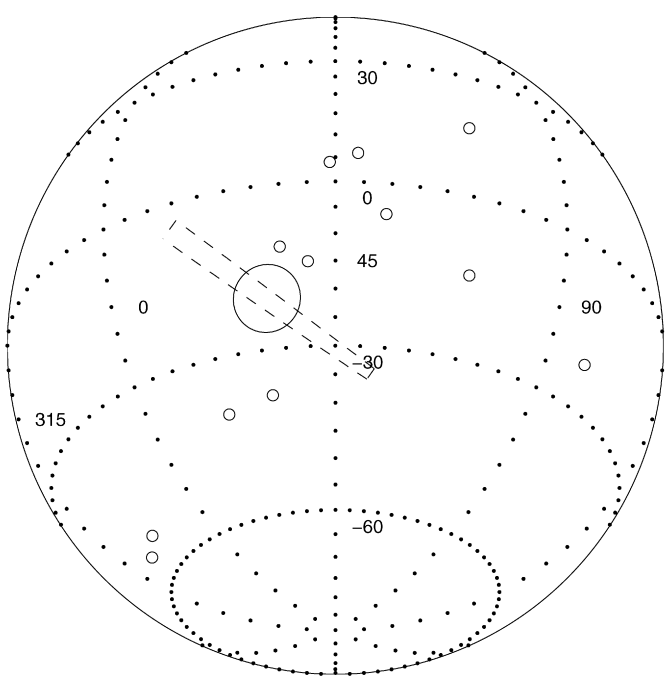

Fig. 5. Pole locations for Pallas on the Ecliptic globe.

position, we consider the pole ambiguity resolved with our observations in conjunction with the locus of pole solutions from lightcurves. Notice that our uncertainty wedge is perpendicular to the spread of the pole estimates, and thus the region of the pole appears to be well delineated. Our rejected ambiguous pole at [RA; Dec] = [154; −16], Ecliptic coordinates $[\lambda; \beta] = [163; -25]$, does not fall close to a similar spread through Ecliptic coordinates around [225; +30]. The consensus pole listed by Kryszczynska is 17° from our pole, and thus we agree on the ambiguity resolution.

Our $a/b = 1.08 \pm 0.04$ ratio is comparable to the 1.1 determined from lightcurves, but of course our $b/c = 1.5 \pm 0.5$ is all but useless although it does cover the consensus from lightcurves of $b/c = 1.05$. Future AO observations closer to Pallas' equator should bring the uncertainty in c down considerably. Despite the large uncertainty in c, the IRAS (Tedesco et al., 1992) diameter of 498 ± 19 km is close to our average diameter, $(abc)^{1/3} = 494 \pm 57$ km.

3.4.2. 3 Juno

Juno is a large S type asteroid (IRAS diameter $= 234 \pm 11$), with apparent ellipse diameters from a stellar occultation of $290 \pm 2 \times 246 \pm 4$ km (Millis et al., 1981). Its 7.21 h lightcurve amplitude varies between 0.14 and 0.22 magnitudes. Magnusson (1986) found a unique rotational pole at [RA; Dec] = [123; +61], which fit the occultation observation for $a = 300$, $b = 249$, $c = 244$ km.

All of the observations for both runs were made with the K_S filter, except that the first night observations in 2004 were made in the J band. Triaxial ellipsoid results from the two dates are given in Tables 4 and 5, and the triaxial solutions are illustrated in Figs. 6 and 7. A weighted mean triaxial ellipsoid model and a weighted mean pole are given in the Summary.

The 2006 observations of Juno were obtained when the asteroid was closer to the Earth, two-thirds the distance for the 2004 observations. Thus the apparent size of the asteroid was 50% larger and more clearly distinguishable from the PSF, which remained basically unchanged since the same telescope and AO system were used, permitting a cleaner separation of the two components with PBD. The apparent size of the asteroid was comparable to the PSF for the 2004 observations but significantly larger for the 2006 observations. The fact that the triaxial ellipsoid model sizes for both epochs are similar gives confidence in the technique even when the asteroid is barely resolved.

The agreement with previous work on Juno is good. As compiled by Kryszczynska, her synthesis or consensus axial ratio of $a/b = 1.2$ is close to our mean value of $a/b = 1.26 \pm 0.03$. Her consensus $b/c = 1.3$ reflects more recent work, but Magnusson (1986) found $b/c = 1.02$, which is more in agreement with our

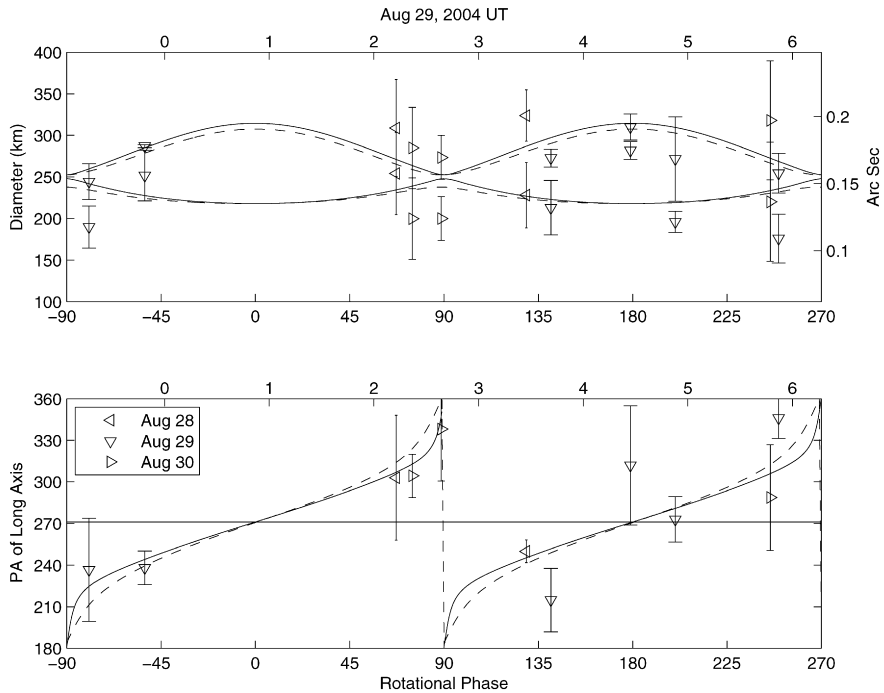

Fig. 6. Triaxial ellipsoid fit for Juno in 2004. In the upper subplot, each image's apparent long and short diameters are plotted with different symbols for each date. The Lorentzian sizes, with a mean diameter of $0.15'' \pm 0.01$, are not plotted because they are comparable to the size of the asteroid. The lower subplot shows that the position angle of the long axis rotates smoothly through 360°, but the line is broken at rotational phase 90° to reduce the scale of the plot. The position of the line of nodes, 90° from the direction to Juno's pole, is shown as a straight line at 271°. Rotational phase zero corresponds to August 29, 2004, 0.868 UT (lighttime corrected), using a rotational period of 7.21 h to fold the observations together.

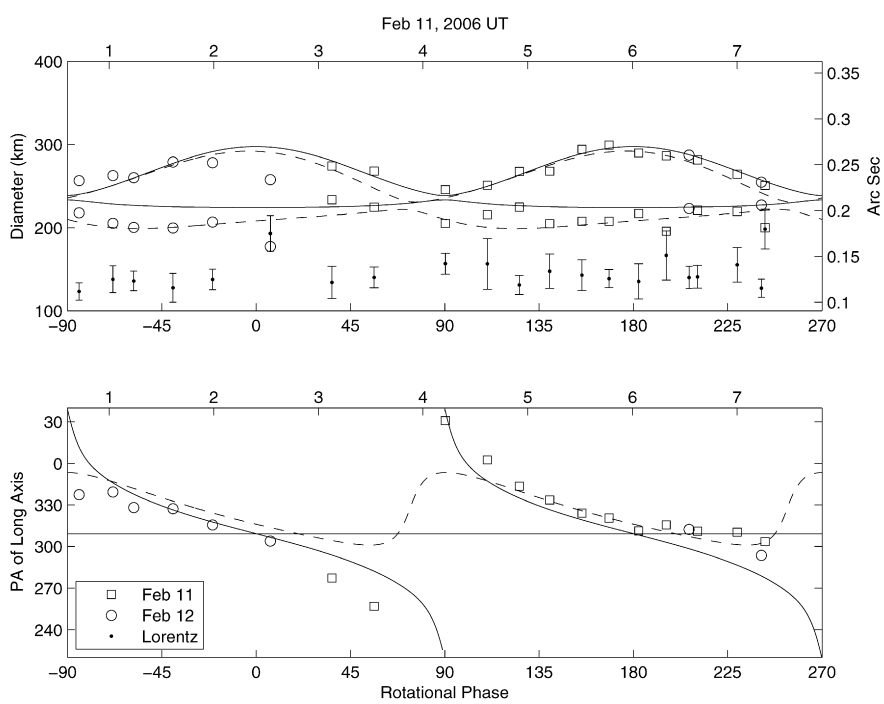

Fig. 7. Same as previous figure, but for Juno in 2006. Compared to Fig. 6, the measured parameters are much better determined in 2006 (error bars are the size of the symbols) than in 2004 because the asteroid is considerably larger than the PSF (dots with error bars plotted along the bottom of the upper subplot). The most discrepant measurement at rotational phase 0° occurs when the PSF suddenly became large and the final triaxial fit is made without this observation. Across the lower subplot, the position of the line of nodes is 309°. Rotational phase zero corresponds to February 11, 2005, 2.403 UT (lighttime corrected), using a rotational period of 7.21 h to fold the observations together.

$b/c = 1.07 \pm 0.03$. Furthermore, the dimensions derived by Magnusson from a stellar occultation ($300 \times 249 \times 244$ km) are very near our mean dimensions ($298 \times 237 \times 222$), the only discrepancy being that we find a slightly smaller b and c.

The two-fold ambiguity for the location of the pole associated with PBD from one date is broken with similar observations from two dates. The two poles in Table 4 are 24° apart, but the other two rejected poles, at [RA; Dec] = [100; −39] for 2004 and

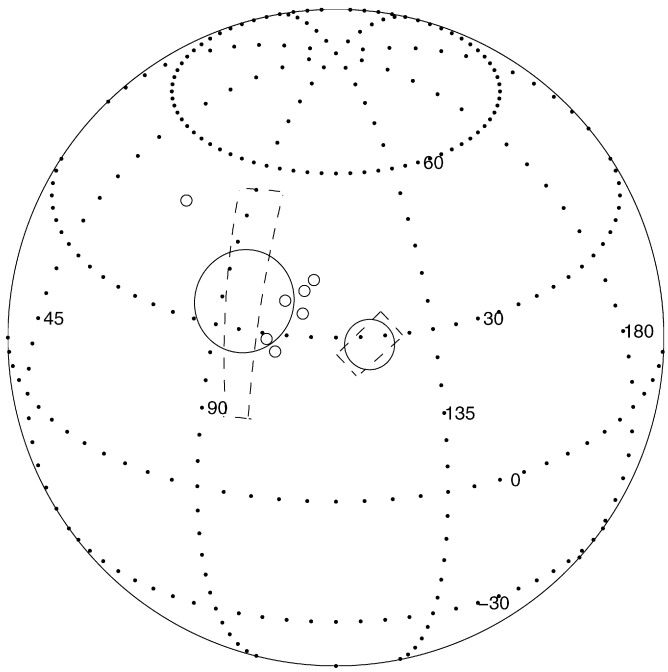

Fig. 8. Pole locations for Juno on the Ecliptic globe. Our pole determined from 2004 is to the left of the pole determined in 2006.

[28; −40] for 2006, are 54° apart. For Juno, there is no fourfold ambiguity usually inherent in lightcurve analysis because the epoch method clearly pins down a pole in the area that we determine from only our observations. The lightcurve consensus pole at [114; +56] lies only 11° from our mean pole given in the Summary. Fig. 8 shows the location of all poles on the Ecliptic globe.

Baliunas et al. (2003) obtained AO images of Juno in 1996 with the 100 in telescope at Mount Wilson, from which they deduced a major albedo feature on the asteroid, a large dark region visible at 0.83 and 0.93 μm wavelengths, much shorter than our observations. No detailed comparison between our AO images and theirs can be made because they did not provide orientation or scale information for their images. It is not clear where in our observations in Figs. 6 and 7 the impact of the large feature might be seen, or even if any impact is to be expected since they attribute the albedo feature to the 0.93 μm olivine and pyroxene absorption band.

3.4.3. 4 Vesta

The Asteroid Vesta is a large well-observed asteroid. It has one lightcurve maximum and minimum during its 5.342 h rotational period, which is dominated by a dark hemisphere. It was observed through the HI filter over three nights in 2004 and two in 2006.

The dimensions and pole from the two dates are given in Table 3 and the triaxial ellipsoid fits are shown in Figs. 9 and 10. The large amplitude of the variation of the position angle of the apparent long axis in 2006, shown in the bottom subplot of Fig. 10, causes the fit to arrive at a very uncertain small c diameter and a very high Earth sub-latitude, θ. If we assume instead that $\theta = 21°$ as predicted by the HST pole of Thomas et al. (1997, Note added in Proof) for the position of Vesta on February 11, 2006, then c can be derived from the apparent small axis length, β. At rotational phase zero, $\beta^2 = b^2 \sin^2\theta + c^2 \cos^2\theta$, and at rotational phase 90° $\beta^2 = a^2 \sin^2\theta + c^2 \cos^2\theta$. Using the β's from the fit in Fig. 10, but $\theta = 21°$, the mean c can be calculated from these expressions as 442 ± 7 km. The fit is shown in Fig. 11 with this c and θ.

Part of the reason for such a large discrepancy undoubtedly lies in the fact that Vesta's southern hemisphere is mottled and may have a large flat region (Thomas et al., 1997), thus departing from the assumption of a smooth, featureless, triaxial ellipsoid. Since in 2004 the sub-Earth latitude was well into Vesta's southern hemisphere for our observations (−27° according to Table 4 or −15° for the HST pole), and the results were good, but in 2006 the sub-Earth latitude was +21° with the HST pole, and the results were bad, it appears that when the far southern regions on Vesta are

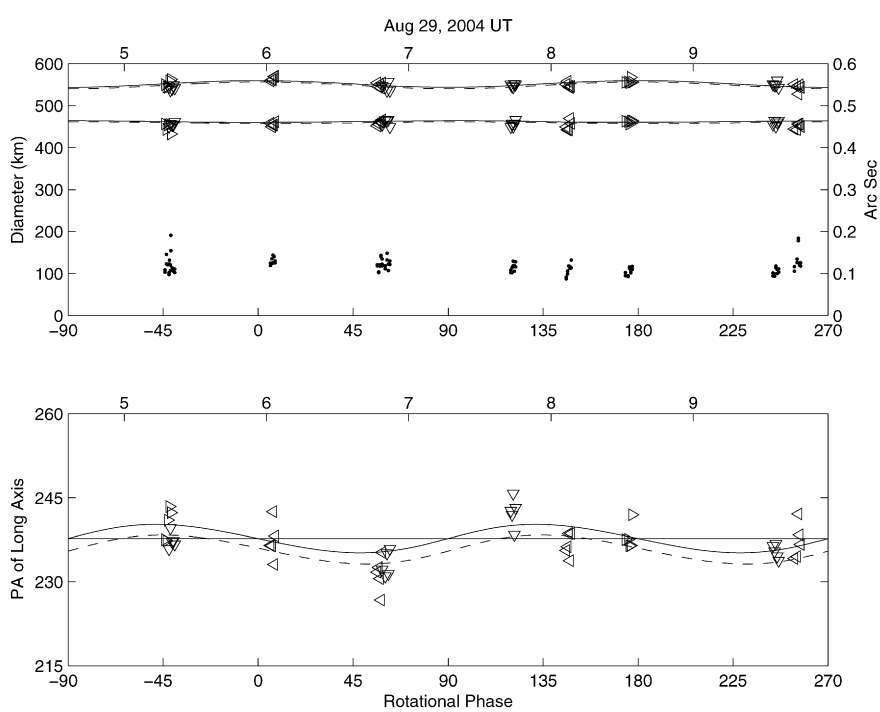

Fig. 9. Triaxial ellipsoid fit for Vesta in 2004. Left, down, and right pointing triangles are from August 28, 29, and 30, respectively. The small dots along the bottom of the upper subplot are the diameters of the Lorentzian PSFs. The straight line across the lower subplot marks the position of the line of nodes at 238°, 90° from the direction to Vesta's pole. Rotational phase zero corresponds to August 29, 2004, 5.941 UT (lighttime corrected), using a rotational period of 5.342 h to fold the observations together.

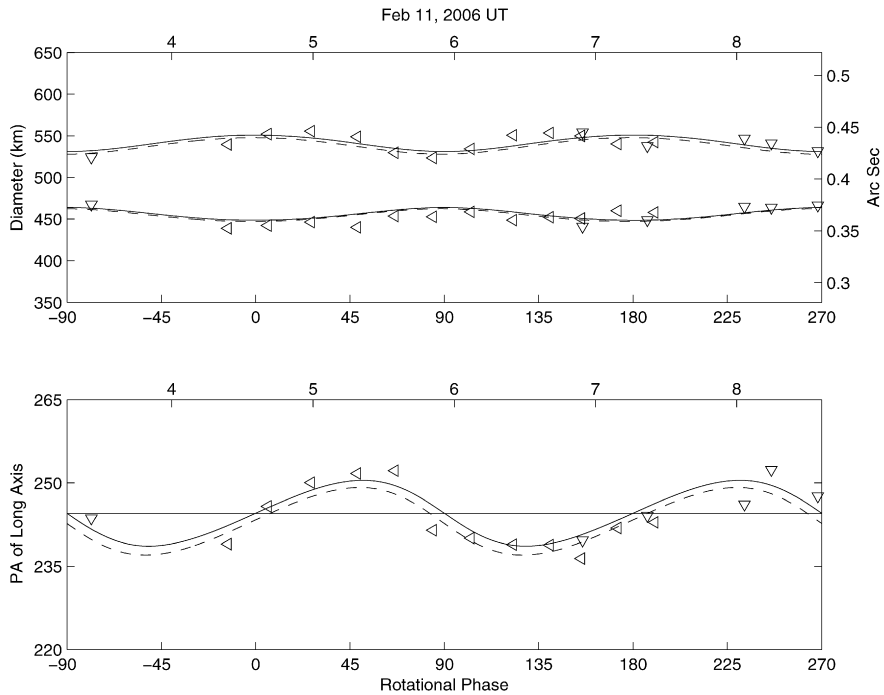

Fig. 10. Same as previous figure, but for Vesta in 2006. Leftward pointing triangles denote data from February 11, and downward from February 12, 2006. The straight line across the lower subplot marks the position of the line of nodes at 245°. The large amplitude of variation for the position angle of the long axis in the lower subplot leads to the unrealistically small and uncertain c dimension and a high sub-Earth latitude, θ. See text. Rotational phase zero corresponds to February 11, 4.473 UT (lighttime corrected), using a rotational period of 5.342 h to fold the observations together.

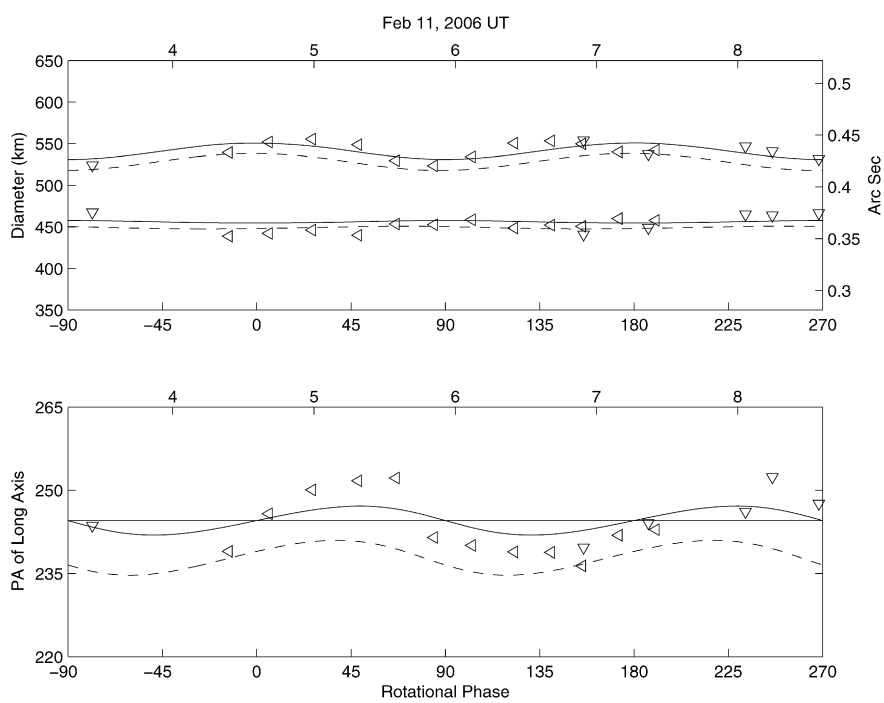

Fig. 11. Same as previous figure for Vesta in 2006, but using the HST predicted (Thomas et al., 1997) sub-latitude for the Earth on this date, $\theta = 21°$. Four of the other six parameters are the same as the model that generated Fig. 10, with the fifth, c, being calculated from these four and the HST θ. See text. These trends in the residuals to the model indicate a departure from the assumptions of the asteroid being a smooth featureless triaxial ellipsoid rotating about its shortest axis.

continually on the limb, they have more of an impact on our observations than when they transit. Furthermore, the solar phase angle was a modest 8.9° in 2004, but 16° in 2006, with the Sun even further north on Vesta than the Earth. Therefore, the sub-Sun latitude on Vesta for 2006 of $= +28°$ would have enhanced the shadowing on the southern limb.

Just as we did for Ceres, we measured 74 images of Vesta (this time with the NICMOS-1 camera) obtained with the HST in 1997 through five filters. The images were furnished by K. Hege and D. McCarthy (personal communication). Fig. 12 shows the fit to this data, where the residuals in the position angles seem quite similar to Fig. 11. For comparison, Vesta's dimensions and pole for

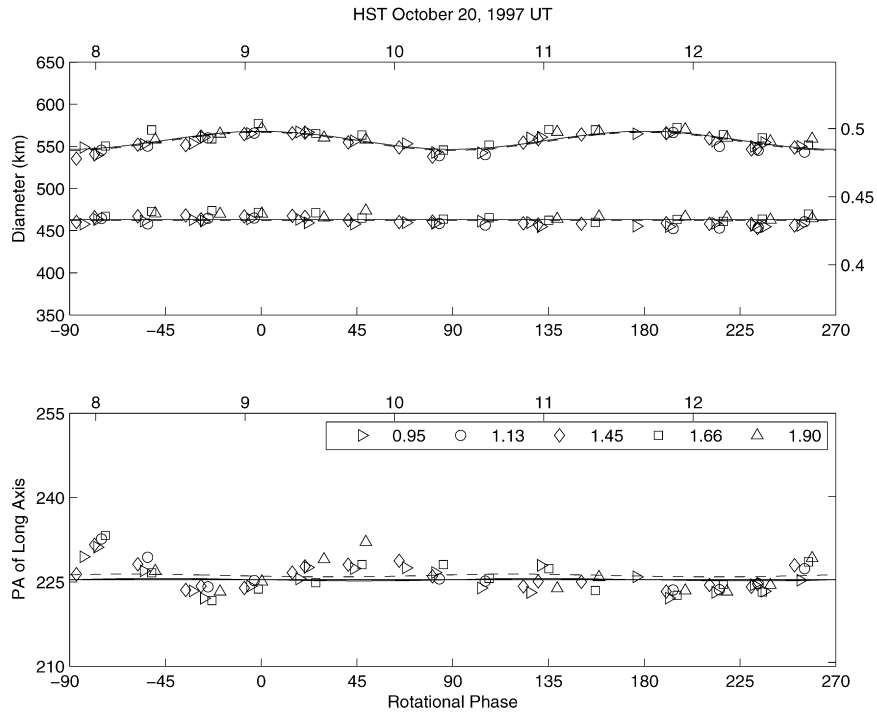

Fig. 12. Triaxial ellipsoid fit for Vesta in 1997, HST observations. The legend shows the wavelength of the observations in microns. The straight line across the lower subplot marks the position of the line of nodes at 225°, 90° from the direction to Vesta's pole. The triaxial fit yields $\theta = -2°$ for this date. Rotational phase zero corresponds to October 20, 1997, 9.1076 UT (lighttime corrected), using a rotational period of 5.342 h to fold the observations together.

Table 6
Vesta resolved: triaxial dimensions and rotational poles

a (km)	*b* (km)	*c* (km)	Pole (J2000) RA (°)	Dec (°)	Err (°)	Date	Method	Reference
584 ± 16	531 ± 11	467 ± 12	315	+41	3.8	Nov 16, 1983	SI	1
562 ± 14	531 ± 17	466 ± 14	274	+48	7.3	Oct 14, 1986	SI	2
566 ± 6	528 ± 6	402 ± 8	324	+44	2.2	Nov 30, 1990	SI IR	3
519 ± 9	486 ± 12	460 ± 8	300	+32	8.4	Feb 22, 1992	SI IR	3
604 ± 13	539 ± 15	467 ± 25	299	+35	6.9	Sep 20, 1993	AO	4
562 ± 24	542 ± 24	426 ± 24	299	+39	10	Nov 30, 1994	HST Limb Fit	5
560 ± 24	544 ± 24	454 ± 24	308	+48	10	Nov 30, 1994	HST Adopted	5
578 ± 10	560 ± 10	458 ± 10	301	+41	5	1994 + 1996	HST Revised Adopted	6
563 ± 3	534 ± 3	402 ± 5	332	+42	1.5	Apr 27, 1996	AO	4
571 ± 2	544 ± 2	434 ± 4	335	+45	0.8	May 11, 1996	AO	4
537 ± 4	509 ± 4	412 ± 8	275	+42	2.0	Oct 18, 1997	AO	7
568 ± 1	547 ± 1	463 ± 1	300	+45	0.7	Oct 20, 1997	HST	8
559 ± 2	543 ± 2	436 ± 18	321	+40	1.6	Aug 29, 2004	AO	8
555 ± 12	531 ± 6	221 ± 622	294	+8	7.5	Feb 11, 2006	AO	8
563 ± 5	534 ± 5	442 ± 7	306	+38	6.7		Mean	

References: 1. Drummond et al. (1988a); 2. Drummond and Hege (1989); 3. McCarthy et al. (1994); 4. Drummond et al. (1998); 5. Thomas et al. (1997); 6. Thomas et al. (1997, Note added in Proof); 7. Drummond (1998); 8. This paper.

all speckle interferometry, AO, and HST observations are listed in Table 6.

Together with the five poles found from lightcurves listed by Kryszczynska, all rotational poles are shown in Fig. 13. The average dimensions in Table 6 are computed as the unweighted mean of all fourteen estimates, with the exception that our 2006 *c* dimension is not used, and the uncertainty is calculated as the error of the mean. However, the mean pole is found by taking the weighted average pole for each of the four techniques, and then computing the unweighted average of the four techniques because it is difficult to intercompare errors from each technique.

3.4.4. 16 Psyche

Because it is bright M class asteroid, with a rotational period (4.196 h) that allows its entire rotation to be followed easily during one night, Psyche has been well observed. From IRAS its diameter is 253 ± 4, and its rotational pole and axial ratios have been estimated many times as can be seen in the compilation of such parameters by Kryszczynska.

We observed Psyche in the K band on two nights in 2004, and on one night in 2006 when we increased the density of observations during a single rotation. Even though it was 1.3 times closer to the Earth in 2004 than in 2006, its short axis in 2004 was comparable to the PSF. In 2006, although further, both apparent axes were larger than the PSF for two reasons: the AO performed better, producing a smaller PSF, and Psyche presented a larger apparent small axis since we observed closer to its pole. Tables 4 and 5 give the results, Fig. 14 shows the data and fit for 2004, and Fig. 15 for 2006. As we did for Vesta, we show all of the measured data rather than the mean of each set of five observations as we did for Pallas and Juno.

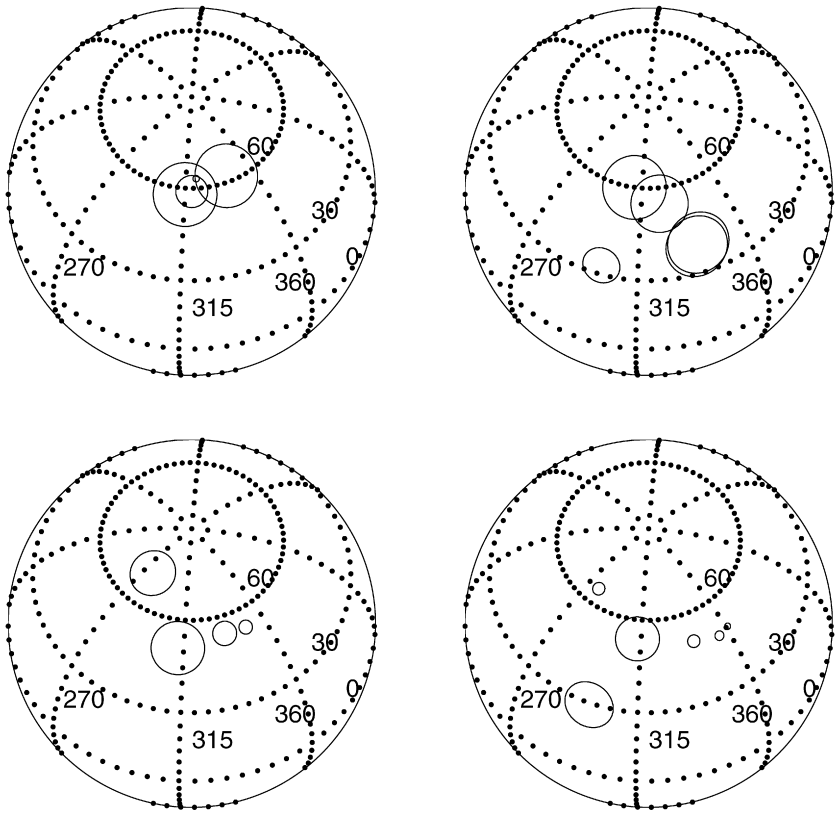

Fig. 13. Vesta's rotational pole locations. Plotted on Ecliptic globes are the locations of Vesta's poles from four techniques. At upper left are the four poles found from HST observations, at upper right are five poles from lightcurve techniques as listed by Kryszczynska, at lower left are four poles found from speckle interferometry observations as listed by Drummond et al. (1998), and at lower right are six poles found from AO observations. Around each pole is the uncertainty circle according to the authors.

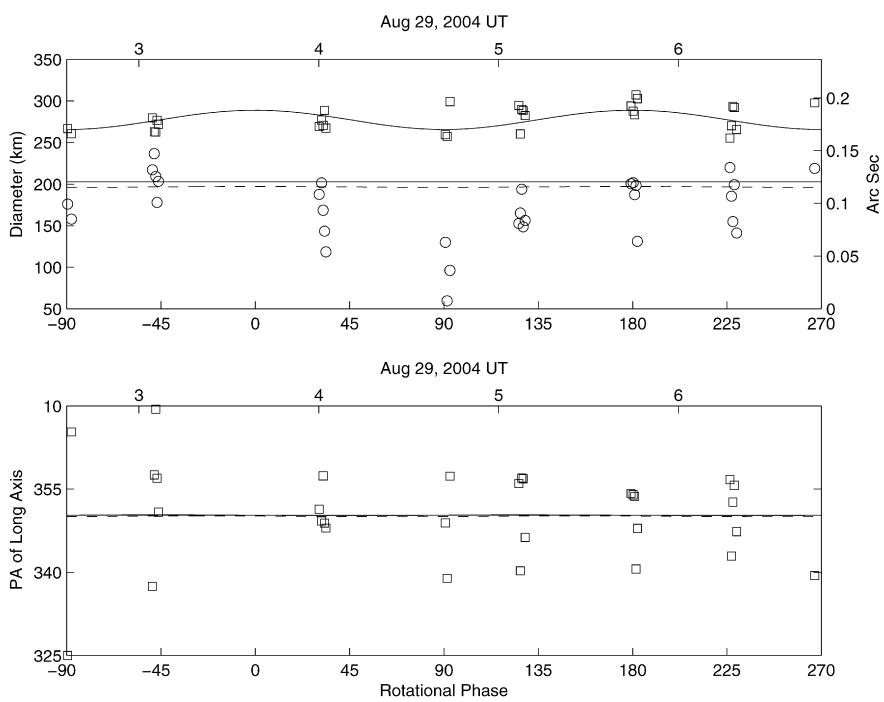

Fig. 14. Triaxial ellipsoid fit to measured ellipse parameters for Psyche in 2004. In the upper subplot, each image's apparent long (squares) and short (circles) diameters are plotted. The PSF Lorentzian diameters, with a mean of $0.12'' \pm 0.04$, are comparable to the short axis dimensions, and so are not plotted. In the lower subplot, the position angle of the long axis barely varies around the line of nodes at 350° because the observations are in the equatorial plane. Rotational phase zero corresponds to August 29, 2004, 3.827 UT (lighttime corrected). The set of observations that straddle rotational phase −90/270 are from August 30, and are folded back with a rotational period of 4.196 h.

Since the two sets of observations were at such different aspects, the normal two-fold rotational pole ambiguity associated with a single set of observations is easily resolved. The possible poles obtained for 2004 were at [RA; Dec] = [36; +9] and

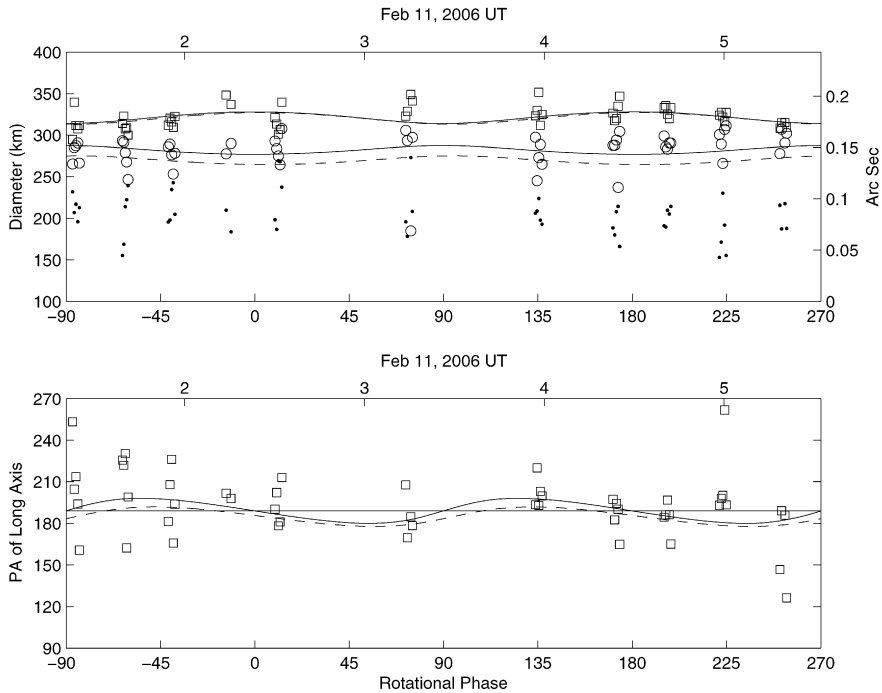

Fig. 15. Same as previous figure, but for Psyche in 2006. Since the asteroid is larger than the PSF, the Lorentzian diameters are plotted (dots), along with the major (squares) and minor (circles) asteroid diameters. In the lower subplot, the position angle of the long axis varies around the line of nodes at 189°. Rotational phase zero corresponds to February 11, 2006, 2.396 UT (lighttime corrected). All the observations were taken on the same night.

[218; −10], while for 2006 they were at [31; +20] and [106; +10]. Kryszczynska lists two possible retrograde poles for Psyche, with the epoch method having eliminated the other two possible prograde poles. Our pole lies between the prograde and retrograde poles on the same Ecliptic longitude, although slightly closer to the retrograde solutions. Since our two poles lie near the Ecliptic equator, we hesitate to even use the term prograde or retrograde. However, we consider the ambiguity resolved in favor of her pole at [38; −1], rather than [210; −23]. The various poles in this section of the sky (in Ecliptic coordinates) are shown in Fig. 16. None of the poles quite satisfy the radar constraints (Magri et al., 1999) shown in Fig. 16, although our error wedge does penetrate the annulus. Coincidentally, the position of Psyche, which was the nearly the same for both sets of radar observations in 1980 and 1985, coincides with our 2006 observations.

Kryszczynska lists the axial ratios for Psyche as $a/b = 1.25$ and $b/c = 1.25$, but most workers found a greater b/c ratio than what she lists as the synthesis. However, our weighted model gives both a smaller a/b ratio of 1.00 ± 0.02 and a greater b/c ratio of 1.54 ± 0.03. These large difference may be due to the difficulty in interpreting the rather asymmetric lightcurves, including the disappearance of one extrema at high sub-Earth latitudes (see Drummond et al., 1988b).

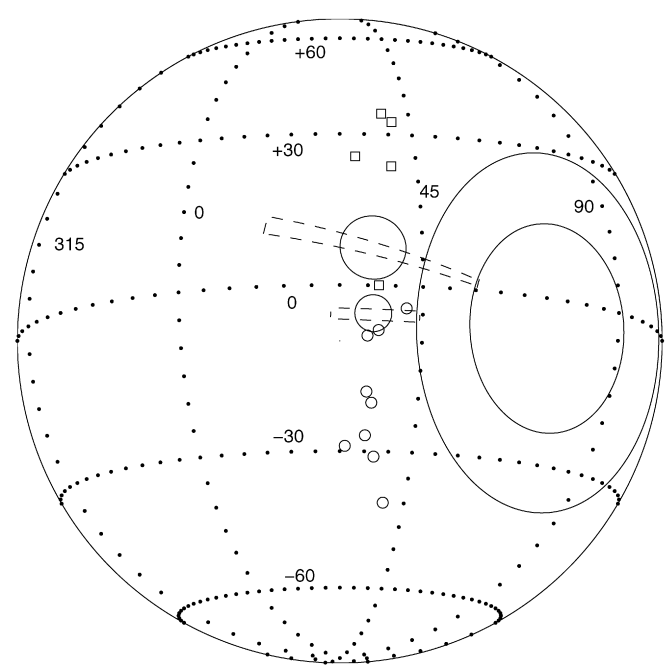

Fig. 16. Pole locations for Psyche on the Ecliptic globe. The squares in this case denote prograde poles from Kryszczynska, while the small circles denote retrograde poles, preferred among those workers who chose between the two. The two largest circles depict the constraints given by radar in which the pole must lie between the inner and outer circles. Our two poles (upper for 2006 and lower for 2004) penetrate the annulus only if their wedge shaped error limits are used.

3.4.5. 87 Sylvia

Sylvia has a short rotational period (5.184 h) that allows its entire rotation to be followed during one night. The epoch method has reduced the pole ambiguity to positive Ecliptic latitudes in two regions, and recent work has reduced it further to just one region. Although Sylvia is known to have two small satellites, our exposure times were not long enough to detect any of them. From IRAS, its diameter is 261 ± 13, and the axial ratios from Kryszczynska are $a/b = 1.42$, $b/c = 1.05$ to 1.5.

All of the fits to the 10 s observations are plotted in Fig. 17, with the triaxial ellipsoid fit results listed in Tables 4 and 5. We resolve our two-fold pole ambiguity with the help of lightcurve techniques. Our preferred pole is only 19° away from the Kryszczynska consensus pole at [RA; Dec] = [68; +78], while our rejected pole lies in the southern hemisphere at [RA; Dec] = [199; −31], well away from the other possible consensus pole at [287; +26] in the northern hemisphere. Fig. 18 shows the Ecliptic coordinates of all of the pole determinations. Kryszczynska's consensus a/b axial ratio of 1.42 is close to our 1.33 ± 0.10 and our b/c ratio of

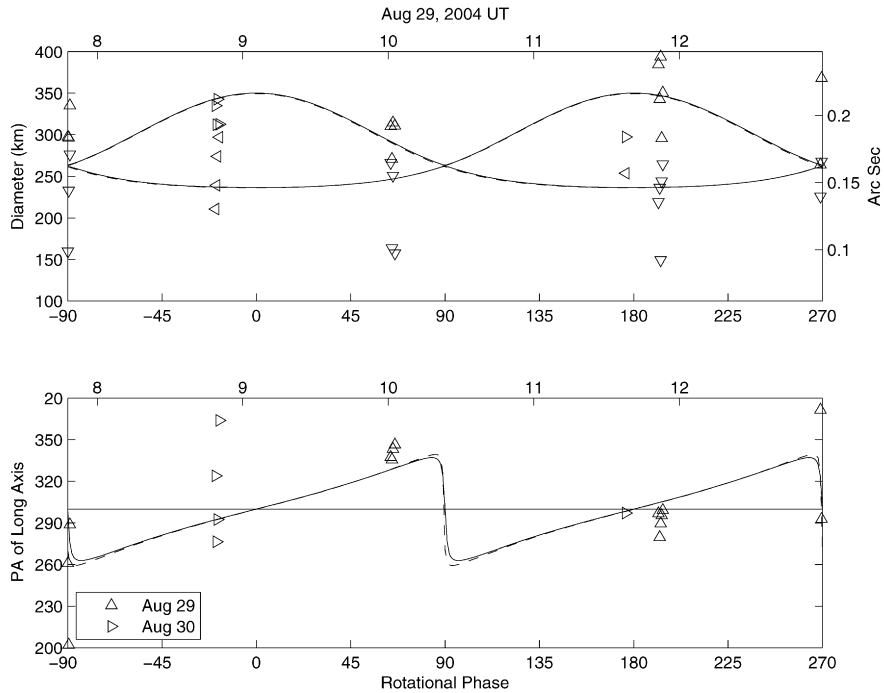

Fig. 17. Triaxial ellipsoid fit for Sylvia. The mean Lorentzian PSF diameter (not plotted) was $0.17'' \pm 0.03$, between the long (upward and right pointing triangles) and short (downward and left pointing triangles) axes of the asteroid. In the lower subplot, the position angle of the long axis varies around the line of nodes at 300°. Rotational phase zero corresponds to August 29, 2004, 9.094 UT (lighttime corrected), using a rotational period of 5.184 h to fold the observations together.

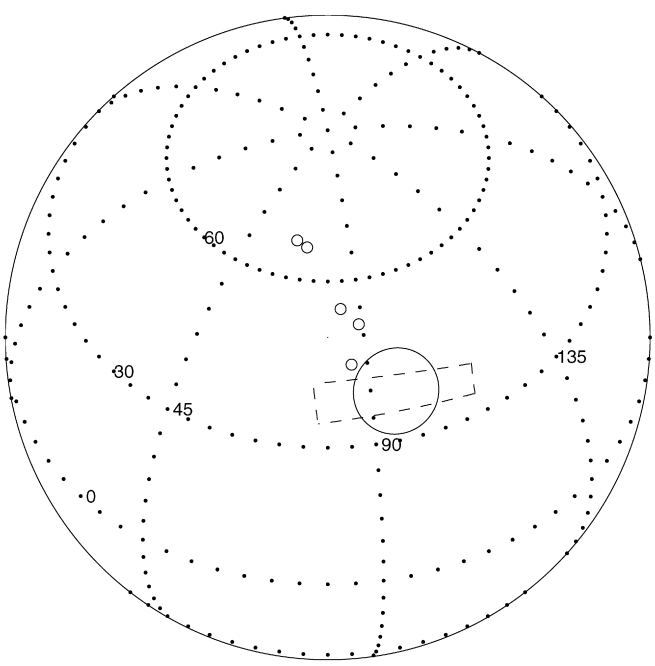

Fig. 18. Pole locations for Sylvia on the Ecliptic globe.

1.16 ± 0.18 is within the range of 1.05 to 1.5. The mean diameter of $(abc)^{1/3} = 276 \pm 15$ is also in agreement with the IRAS diameter.

3.4.6. 324 Bamberga

The Asteroid Bamberga is a large asteroid (diameter from IRAS is 229 ± 7 km) with a low 0.07 magnitude amplitude lightcurve and a long 29.43 h period (Gehrels and Owings, 1962; Scaltriti et al., 1980). However, because it is a dark (albedo $= 0.063 \pm 0.004$) C type asteroid, it has not been observed very often, and there are no published axial ratios or rotational poles.

The small number of observations (4) and poor rotational phase coverage, made it difficult to find a good least squares fit to the data. In fact, the data from one epoch had to be thrown out, as illustrated in Fig. 19, and a triaxial ellipsoid fit that is consistent with the two lightcurves could not be found. Furthermore, neither of the possible poles from the triaxial ellipsoid fit satisfies the constraint found from radar (Magri et al., 1999), that the rotational pole lies within 40° of the south Ecliptic pole. See Fig. 20.

If, instead, we adopt a biaxial ellipsoid assumption, $b = c$, then a solution can be found that satisfies both the lightcurve and radar data. One of the two poles obtained from the fit yields similar sub-Earth latitudes of +34° and −30° for the positions of both lightcurve observations. From just the ratio of our model projected areas at maximum and minimum, the predicted amplitudes for the two lightcurves are 0.05 and 0.06, which if increased by a solar phase angle/amplitude relation, would match the observed 0.07 magnitude amplitudes. This biaxial solution is given in Table 4, and the pole in Table 5 lies 28° from the south Ecliptic pole, satisfying the radar constraint. Thus, the usual two-fold pole ambiguity inherent in our solution is resolved by consideration of the lightcurves and radar observations, with the rejected pole located at [RA; Dec] = [337; +67].

Note that the 20° solar phase angle for our observations is among the largest for an asteroid studied this way. This caused the Sun terminator to have a profound effect on fitting the data. Most of the information about this nearly round asteroid is carried by the changing position angle, pa_{α_S}, of the Sun's terminator ellipse long axis. In Fig. 19, notice how the asteroid's long axis position angle, pa_{α_A}, rotates through a full 360°, while the Sun's terminator ellipse long axis does not.

Fig. 20 shows the Ecliptic globe with the error circle around our pole along with the more proper wedge shape error boundary. Also shown is the annulus where radar observations place the pole.

In 2006, the asteroid, although at opposition, was a magnitude fainter and 1.7 times further than in 2004. Based on its size from Table 3, its predicted apparent diameter was the same as the diffraction limit, and in fact the two data sets of five obser-

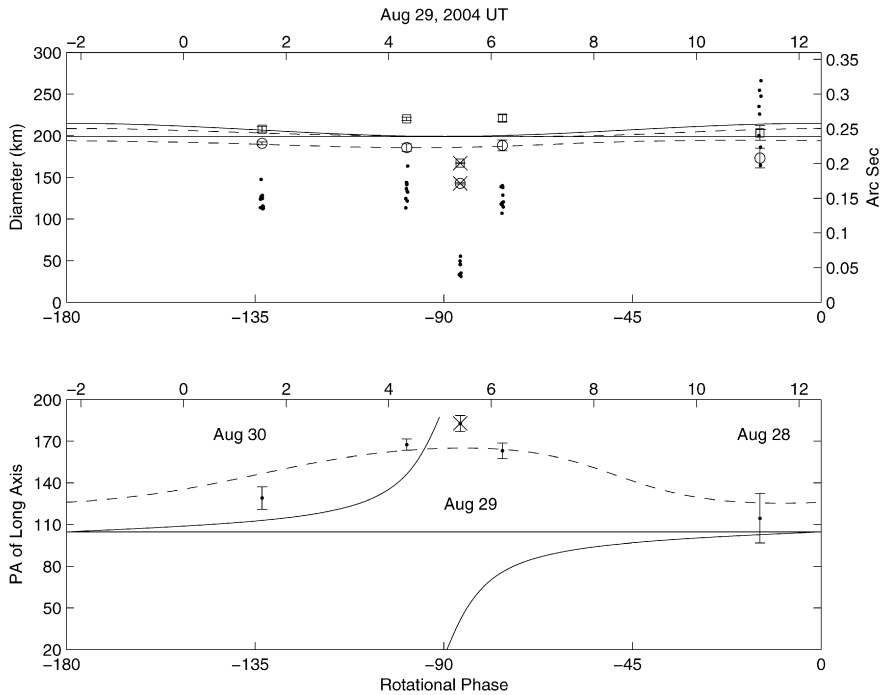

Fig. 19. Biaxial ellipsoid fit for Bamberga. The measured major axes diameters are denoted by squares, the minor axes by circles, and the Lorentzian PSF diameters by dots in the upper subplot. Notice that only half of the full rotation is depicted, unlike the scale for all other such figures. One set of data was not used in the fit and is ×'ed over. The biaxial solution satisfies Bamberga's lightcurve history and radar constraint. In the lower subplot, the position angle of the long axis varies around the line of nodes at 105°, but notice the difference in behavior between the body's position angle and the terminator's position angle (dashed line) at the large (20°) solar phase angle on this date. Rotational phase zero corresponds to August 29, 2004, 12.4 UT (lighttime corrected), using a rotational period of 29.43 h to fold the observations together.

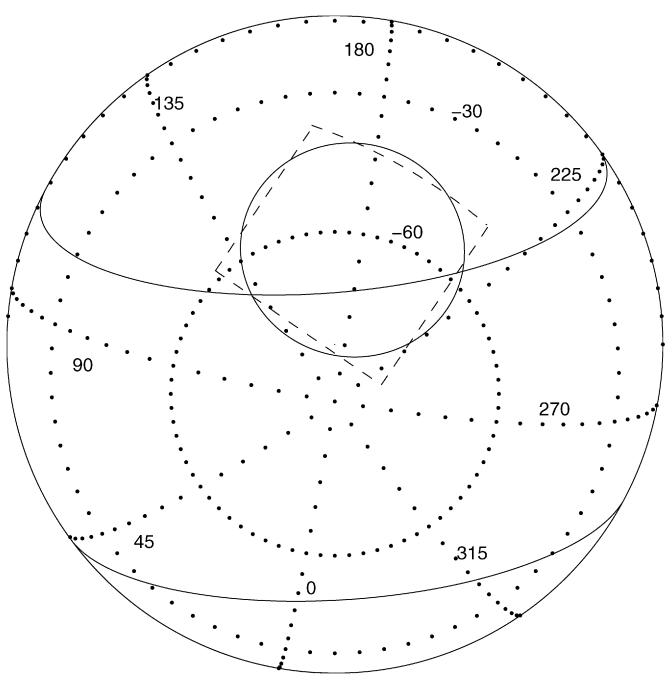

Fig. 20. Location of Bamberga's pole at $[\lambda; \beta] = [177; -62]$ on an Ecliptic globe. Radar constrains the pole to lie within the large annulus, the area between the solid lines that span the globe. Our pole is consistent with this constraint; Bamberga's pole is well south of the Ecliptic.

vations each did not reduce to sensible results. We tried fitting two multi-frame-blind-deconvolution images for just the asteroid Bessel function. We also tried making the standard least squares routine a little more sophisticated by including the expected Airy pattern. Although both extraordinary methods yielded similar results, all we could determine was that indeed Bamberga was comparable to the PSF, consistent with its prediction from the 2004 results, but the measurements were too uncertain to improve those results.

In summary, although we have made the first determination of the location of the coordinates for the rotational pole for Bamberga, overall the results are the weakest for any asteroid in our study. The reasons we were only able to obtain a reasonable solution by adopting a biaxial ellipsoid assumption are probably because of the poor rotational phase coverage possible for Bamberga's nearly 24 h period, the small number of observations used in the fit, and the relatively large solar phase angle. However, the biaxial solution does satisfy both low amplitude lightcurves and the radar constraint.

3.4.7. 704 Interamnia

With only four observations in July 2006, it is surprising that any results (given in Tables 4 and 5 and illustrated in Figs. 21 and 22) are obtained at all for Interamnia. Even though the triaxial ellipsoid parameters contain large uncertainties, our two ambiguous poles help break the ambiguity from the handful of pole estimates from lightcurves. The most recent of these (Michalowski et al., 1995), at [RA; Dec] = [41; +39], is only 17° from our pole in Table 4 and shown in Fig. 22, while our rejected pole at [RA; Dec] = [285; −16] is some 50° from the three other pole estimates in that region.

Our $a/b = 1.14 \pm 0.17$ is in agreement with the 1.11–1.19 found from lightcurves, while our $b/c = 2.1 \pm 2.3$, as for Pallas, is meaningless, and like Pallas, observations closer to the asteroid's equator should provide a better estimate of the c dimension. The large uncertainty in c prevents any real comparison to the IRAS diameter of 317 ± 5 km, but taking 317 km as a mean diameter and combining this with our a and b implies that c might be closer to 245 km than to the 163 km in Table 3.

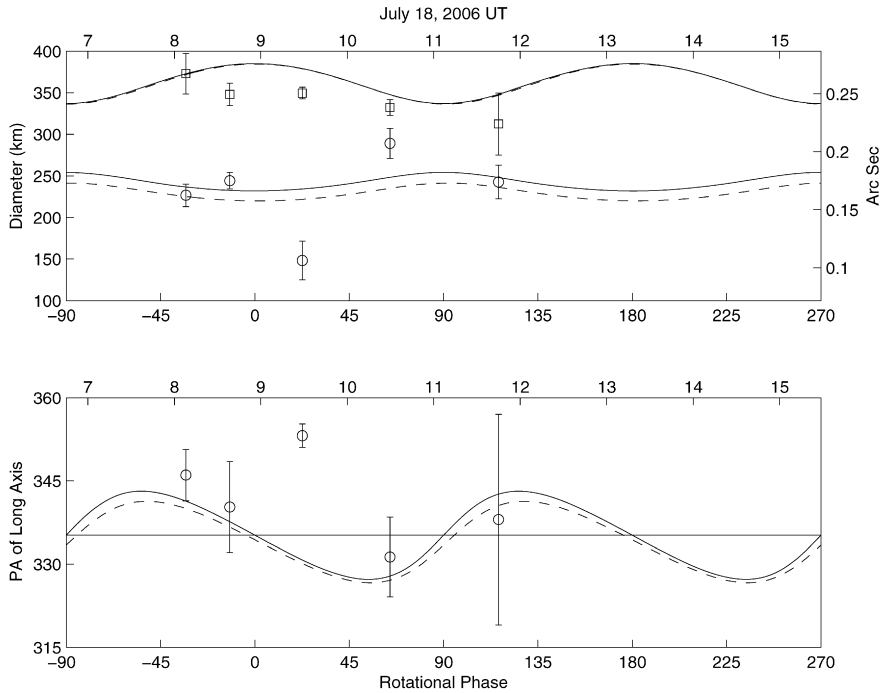

Fig. 21. Triaxial fit for Interamnia. The mean Lorentzian PSF diameter was $0.26'' \pm 0.03$, comparable to the size of the asteroid. In the lower subplot, the position angle of the long axis varies around the line of nodes at 335°. Rotational phase zero corresponds to July 18, 2006, 8.926 UT (lighttime corrected), using a rotational period of 8.727 h.

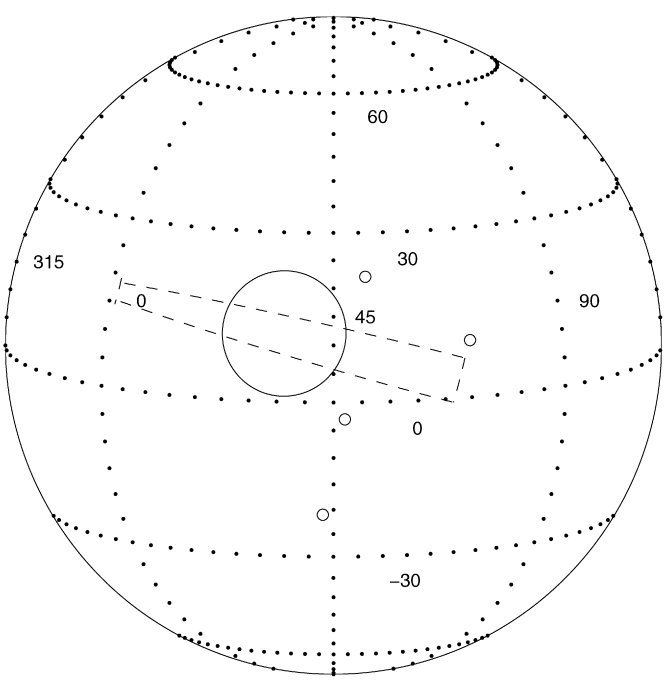

Fig. 22. Pole locations for Interamnia pole on the Ecliptic globe.

Table 7
Summary of asteroid ellipsoid diameters and poles

Name	a (km)	b (km)	c (km)	RA	Dec	Err	Rad	Lon	Lat	Notes
1 Ceres	973 ± 7	973 ± 7	908 ± 9	293	+63	4	352	+80	2
2 Pallas	594 ± 17	549 ± 15	369 ± 128	37	−7	6	32	−21	1
3 Juno	298 ± 6	237 ± 4	222 ± 6	128	+49	13	118	+30	1
4 Vesta	559 ± 2	542 ± 2	436 ± 18	319	+39	12	341	+51	1
4 Vesta	563 ± 5	534 ± 5	442 ± 7	306	+38	7	325	+55	3
16 Psyche	304 ± 5	303 ± 3	197 ± 4	35	+11	7	36	−3	1
87 Sylvia	350 ± 19	264 ± 14	227 ± 33	100	+62	8	96	+39	1
324 Bamberga	215 ± 15	199 ± 7	199 ± 7	142	−53	20	177	−62	1
704 Interamnia	385 ± 53	337 ± 21	163 ± 184	29	+25	11	36	+12	1

Notes: 1. Lick Observatory only data (this paper); 2. Non-Lick observations; 3. Summary from all observations (Table 6).

4. Summary

Table 7 summarizes the results from this study of asteroids resolved with AO on the 3 m Shane telescope at Lick Observatory, listing equatorial and Ecliptic coordinates for the spin axes, and the ellipsoid diameters in km. Where an asteroid is observed on two dates, weighted means are computed and the uncertainties are the weighted error of the means. Except for Vesta, which spanned more than 7 pixels on the camera, all of the asteroids, although resolved in both directions, were only between 1.5 and 3.4 pixels. Fig. 23 shows the model of each asteroid at a rotational phase of 45°, midway between maximum and minimum projected area, and the diameters of the Lorentzian PSF at the time of the observations, projected to the distance to the asteroid. Table 7 also includes the results for Ceres, which we did not observe, and a summary model for Vesta.

Assuming that Ceres is an oblate spheroid, we have demonstrated how resolved images at more than one opposition can yield its rotational pole and dimensions. Our parametric blind deconvolution technique yielded good results (±3%) for the a and b diameters of Pallas, but a c dimension with an uncertainty of 17%. In conjunction with the poles found from lightcurves, its pole ambiguity is resolved. Juno was observed at two oppositions, and therefore the normal two-fold ambiguity inherent in our technique is resolved, and is consistent with the resolution of the ambiguities from lightcurves reported by Kryszczynska. Vesta, being large and bright, yielded one set of good results in 2004 and one of poor results in 2006, when apparently its mottled and deformed southern hemisphere produced small but fatal variations in the observed position angle of the apparent ellipses. However, the weighted mean model stands in good agreement with 12 other high resolution results.

With our observations of Psyche at two epochs we have resolved its pole ambiguity. However, our estimates of its nearly equal equatorial dimensions imply that it should exhibit a low am-

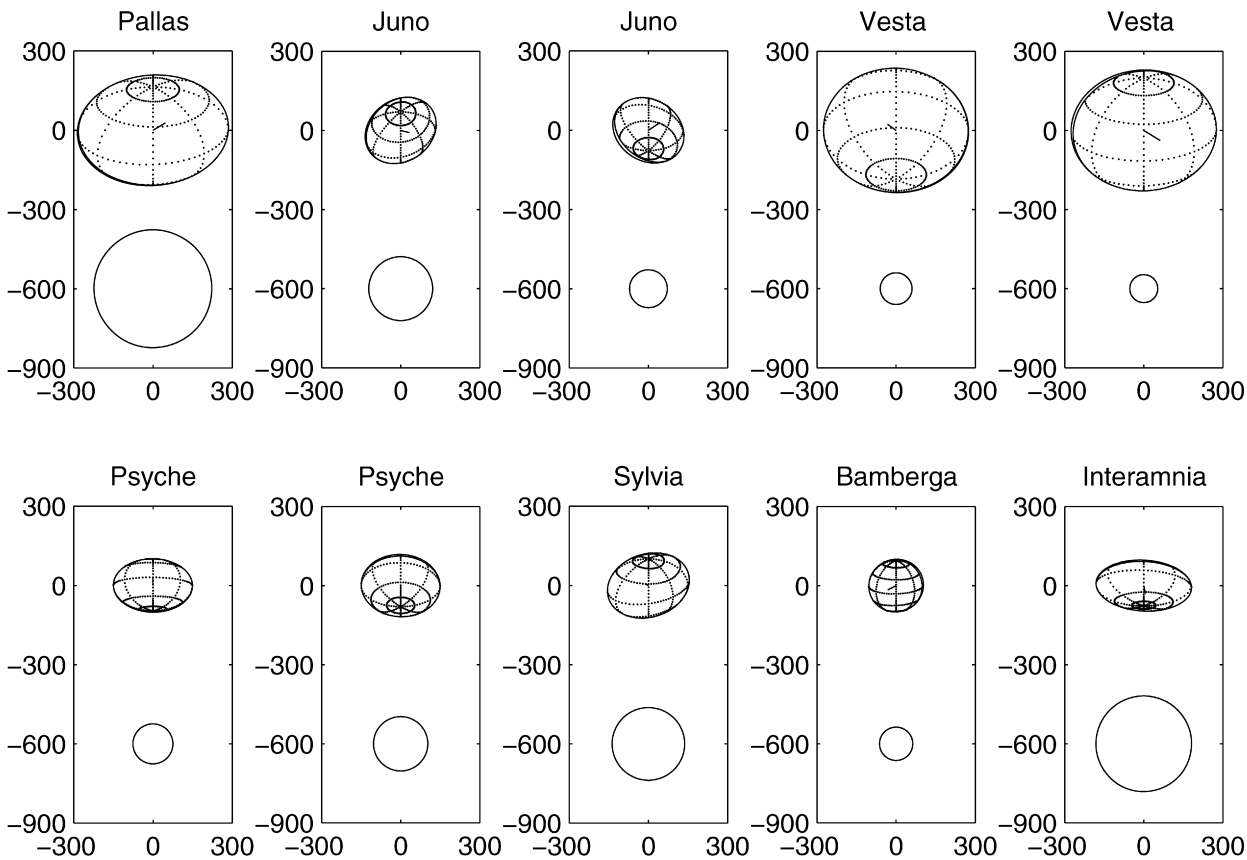

Fig. 23. Models of the asteroids. To the same scale in km, all asteroids are shown at rotational phase $\psi = 45°$, that is, 45° after maximum projected area, and at the sub-Earth latitude of the observations. The sub-Earth and sub-Sun points are connected by a line. The circle beneath each asteroid represents the Lorentzian PSF FWHM.

plitude lightcurve. Therefore, its up to 0.25 magnitude lightcurve amplitude is most likely caused by albedo features, a distorted shape, or both. Despite observations at only five points in its rotation, the results for Sylvia are in good agreement with previous work, with some systematic residuals indicating departure from a pure triaxial ellipsoid shape. Its pole ambiguity is resolved by combining our results with the poles found from lightcurves. Bamberga was the most difficult to interpret, but in order to match the few available lightcurves and a radar constraint we had to discard the triaxial ellipsoid solution in favor of a prolate spheroid solution, which then gives the first-ever pole and ellipsoid dimensions for this large, dark, and slowly backwards rotating asteroid. With only four observations on one night, the uncertainties in the model derived for Interamnia are larger than most of the other asteroids, but its pole is now resolved with the help of the few poles from lightcurves.

While lightcurves are extremely valuable, poles can only be obtained after lightcurves are gathered from many oppositions, sometimes spanning decades, and only yield axial ratios. Our PBD method, however, gives dimensions, rather than axial ratios, and a pole to within a two-fold ambiguity in only one or two nights, and a full pole resolution with images from two epochs.

The results presented in this paper illustrate the limits of what the analysis can extract from limited spatial resolution data. Clearly, significantly improved estimations of an asteroid's size are obtainable with multiple diffraction-limited resolution elements across the disk. The resolution obtained by an adaptive optics system is λ/D where λ is the observing wavelength and D the telescope's effective diameter. For these data, the resolution was limited by the IRCAL camera which is critically sampled for K-band observations and thus under-sampled at H and J where the compensation is also less. Even then the theoretical resolution at J is only approximately a factor of 2 greater than at K. For the smaller asteroids presented here, we require a factor of three in resolution to significantly improve size estimates. This can be achieved by using a higher order AO system on a larger aperture telescope where the asteroids are still bright enough to be used as NGS targets. As an example, 8–10 m class telescopes have apertures three times larger so that in the K-band the effective resolution is three times smaller. The analysis presented here has been already successfully applied to data from Keck (Conrad et al., 2007) clearly demonstrating the improvement of having a larger number of resolution elements across the disk. Preliminary reductions of Keck observations of Pallas have confirmed the pole found here while drastically reducing the uncertainty of the dimensions ($548 \pm 3 \times 504 \pm 3 \times 459 \pm 15$) compared to the values listed in Table 6. Other similar observations have been made at Keck, and still more are planned for other AO systems on large ($\geqslant$8 m) telescopes.

Acknowledgments

We are grateful to Joel Parker for providing the HST data of Ceres taken in 2003, and to Don McCarthy and E. Keith Hege for providing the HST data of Vesta taken in 1997. Two reviewers contributed substantially to improvements in the manuscript. The excellent staff at Lick Observatory is acknowledged for their essential assistance, especially Chris Miller and Ellie Gates. Observational and travel support for Drummond was provided by the Directed Energy Directorate of the Air Force Research Laboratory. This research made use of NASA's Astrophysics Data System and of JPL's Horizons On-Line Ephemeris System.

References

Baliunas, S., Donahue, R., Rampino, M.R., Gaffey, M.J., Shelton, J.C., Mohanty, S., 2003. Multispectral analysis of Asteroid 3 Juno taken with the 100-inch telescope at Mount Wilson Observatory. Icarus 163, 135–141.

Bauman, B.J., Gavel, D.T., Waltjen, K.E., Freeze, G.J., Hurd, R.L., Gates, E.L., Max, C.E., Olivier, S.S., Pennington, D.M., 2002. Update on optical design of adaptive optics system at Lick Observatory. In: Tyson, R.K., Bonaccini, D., Roggemann, M.C. (Eds.), Adaptive Optics Systems and Technology II. In: Proc. SPIE, vol. 4494. SPIE, Bellingham, WA, pp. 19–29.

Carry, B., Dumas, C., Fulchignoni, M., Merline, W.J., Berthier, J., Hestroffer, D., Fusco, T., Tamblyn, P., 2008. Near-infrared mapping and physical properties of the dwarf-planet Ceres. Astron. Astrophys. 478, 235–244.

Christou, J.C., Drummond, J.D., 2006. Measurements of binary stars, including two new discoveries, with the Lick Observatory adaptive optics system. Astron. J. 131, 3100–3108.

Conrad, A.R., and 10 colleagues, 2007. Direct measurement of the size, shape, and pole of 511 Davida with Keck AO in a single night. Icarus 191, 616–627.

Drummond, J.D., 1998. Adaptive optics Lorentzian point spread function. In: Bonaccini, D., Tyson, R.K. (Eds.), Adaptive Optical System Technologies. In: Proc. SPIE, vol. 3353. SPIE, Bellingham, WA, pp. 1030–1037.

Drummond, J.D., 2000. Measuring asteroids with adaptive optics. In: Ageorges, N., Dainty, C. (Eds.), Laser Guide Star Adaptive Optics for Astronomy. Kluwer Academic Publishers, Dordrecht, pp. 243–262.

Drummond, J.D., Hege, E.K., 1989. Speckle interferometry of asteroids. In: Binzel, P.B., Gehrels, T., Matthews, M.S. (Eds.), Asteroids II. Univ. of Arizona Press, Tucson, pp. 171–191.

Drummond, J.D., Cocke, W.J., Hege, E.K., Strittmatter, P.A., Lambert, J.V., 1985. Speckle interferometry of asteroids. I. 433 Eros. Icarus 61, 132–151.

Drummond, J.D., Eckart, A., Hege, E.K., 1988a. Speckle interferometry of asteroids. IV. Reconstructed images of 4 Vesta. Icarus 73, 1–14.

Drummond, J.D., Weidenschilling, S.J., Chapman, C.R., Davis, D.R., 1988b. Photometric geodesy of main-belt asteroids. II. Analysis of lightcurves for poles, periods, and shapes. Icarus 76, 19–77.

Drummond, J.D., Fugate, R.Q., Christou, J.C., Hege, E.K., 1998. Full adaptive optics images of Asteroids Ceres and Vesta; Rotational poles and triaxial ellipsoid dimensions. Icarus 132, 80–99.

Gavel, D.T., Olivier, S.S., Bauman, B.J., Max, C.E., Macintosh, B.A., 2000. Progress with the Lick adaptive optics system. In: Wizinowich, P.L. (Ed.), Adaptive Optical Systems Technology. In: Proc. SPIE, vol. 4007. SPIE, Bellingham, WA, pp. 63–70.

Gehrels, T., Owings, D., 1962. Photometric studies of asteroids. IX. Additional lightcurves. Astrophys. J. 135, 906–924.

Li, J.-Y., McFadden, L.A., Parker, J.W., Young, E.F., Stern, S.A., Thomas, P.C., Russell, C.T., Sykes, M.V., 2006. Photometric analysis of 1 Ceres and surface mapping from HST observations. Icarus 182, 143–160.

Lloyd, J.P., Liu, M.C., Macintosh, B.A., Severson, S.A., Deich, W.T., Graham, J.R., 2000. IRCAL: The infrared camera for adaptive optics at Lick Observatory. In: Iye, M., Moorwood, A.F. (Eds.), Optical and IR Telescope Instrumentation and Detectors. In: Proc. SPIE, vol. 4008. SPIE, Bellingham, WA, pp. 814–821.

Magnusson, P., 1986. Distribution of spin axes and senses of rotation for 20 large asteroids. Icarus 68, 1–39.

Magnusson, P., 1989. Pole determination of asteroids. In: Binzel, P.B., Gehrels, T., Matthews, M.S. (Eds.), Asteroids II. Univ. of Arizona Press, Tucson, pp. 1180–1190.

Magnusson, P., Baruci, M.A., Drummond, J.D., Lumme, K., Ostro, S.J., Surdej, J., Taylor, R.C., Zappala, V., 1989. Determination of pole orientations and shapes of asteroids. In: Binzel, P.B., Gehrels, T., Matthews, M.S. (Eds.), Asteroids II. Univ. of Arizona Press, Tucson, pp. 66–97.

Magri, C., Ostro, S.J., Rosema, K.D., Thomas, M.L., Mitchell, D.L., Campbell, D.B., Chandler, J.F., Shapiro, I.I., Giorgini, J.D., Yeomans, D.K., 1999. Mainbelt asteroids: Results of Arecibo and Goldstone radar observations of 37 objects during 1980–1995. Icarus 140, 379–407.

McCarthy, D.W., Freeman, J.D., Drummond, J.D., 1994. High resolution images of Vesta at 1.65 μm. Icarus 108, 285–297.

Michalowski, T., Velichko, F.P., di Martino, M., Krugly, Y.N., Kalashnikov, V.G., Shevchenko, V.G., Birch, P.V., Sears, W.D., Denshev, P., Kwiatkowski, T., 1995. Models of four asteroids: 17 Thetis, 52 Europa, 532 Herculina, and 704 Interamnia. Icarus 118, 292–301.

Millis, R.L., and 10 colleagues, 1981. The diameter of Juno from its occultation of AG + 0 deg 1022. Astron. J. 86, 306–313.

Millis, R.L., and 41 colleagues, 1987. The size, density, and albedo of Ceres from its occultation of BD + 8°471. Icarus 72, 507–518.

Parker, J.W., Stern, S.A., Thomas, P.C., Festou, M.C., Merline, W.J., Young, E.F., Binzel, R.P., Lebofsky, L.A., 2002. Analysis of the first disk-resolved images of Ceres from ultraviolet observations with the Hubble Space Telescope. Astron. J. 123, 549–557.

Saint-Pe, O., Combes, M., Rigaut, F., 1993. Ceres surface properties by high-resolution imaging from Earth. Icarus 105, 271–281.

Scaltriti, F., Zappala, V., Stanzel, R., Blanco, C., Catalano, S., Young, J.W., 1980. Lightcurves and phase relation of Asteroid 324 Bamberga. Icarus 43, 391–398.

Tedesco, E.F., Veeder, G.J., Fowler, J.W., Chillemi, J.R., 1992. The IRAS Minor Planet Survey—Final Report (PL-TR-92-2049). Phillips Laboratory, Hanscom Air Force Base, MA.

Thomas, P.C., Binzel, R.P., Gaffey, M.J., Zellner, B.J., Storrs, A.D., 1997. Vesta: Spin pole, size, and shape from HST images. Icarus 128, 88–94.

Thomas, P.C., Parker, J.W., McFadden, L.A., Russell, C.T., Stern, S.A., Sykes, M.V., Young, E.F., 2005. Differentiation of the Asteroid Ceres as revealed by its shape. Nature 437, 224–226.